BIELEFELD UNIVERSITY

FACULTY OF PHYSICS

Master's Thesis

Gravitational Lensing and Time Delay

February 26, 2021

Author
Shivani Deshmukh
sdeshmukh@physik.uni-bielefeld.de
Bielefeld University

Supervisor & First Referee
Prof. Dr. Dominik Schwarz
dschwarz@physik.uni-bielefeld.de
Bielefeld University

Second Referee
Dr. Yuko Urakawa
yuko@physik.uni-bielefeld.de
Bielefeld University

Contents

Chapter 1

Introduction

Historical Aspect

A consequence of Albert Einstein's theory of general relativity is gravitational lensing. In recent years the true scope and importance of gravitational lensing as a powerful tool to investigate fields of astronomy and cosmology has been realized. The idea of bending of light rays in the vicinity of massive objects can be found in various times in history. One of the first acknowledgements of it is seen in Isaac Newton's "Optiks" published in 1704. Around 1784, inspired by the correspondence with the British astronomer John Michell, Henry Cavendish calculated the deflection of light using Newton's law of gravitation and the corpuscular theory of light. He never published his calculations, they were only retrieved posthumous when Frank Dyson examined some of his unpublished astronomical papers in 1922. In 1804, the Munich astronomer Johann George von Soldner published a paper along the same lines. The results of Cavendish and Soldner produce the Newtonian deflection of light (Cervantes-Cota et al., 2019).

But only after the conception of general relativity in 1915 was the true deflection angle and nature of light deflection unravelled. The famous 1919 solar eclipse expedition to prove general relativity was the first successful test of the theory. The test correctly measured the light deflection angle of stars in the vicinity of the Sun which corresponded to the calculated value using general relativity. This value differs to the Newtonian value by a factor of 2.

The first mention of gravitational "lensing" was done by Oliver Lodge when he criticized that such a gravitational system has no focal length. Arthur Eddington showed the possibility of occurrence of multiple images in case of a well-aligned system. In 1924, Orest Chwolson worked out the case of formation of ring-like images, called "Einstein rings" (Schneider et al., 1999).

In 1937, Fritz Zwicky made calculations on the observation of gravitational lensing, discussed its importance and applicability. He was the first to realize the major impact it could have on cosmology. To infer the mass distribution of lensing galaxies, magnification of lensed sources which would have been extremely faint otherwise, distance measurement and as probes of the stellar composition of the lenses to name a few applications (Blandford and Narayan, 1992). Zwicky's work was ahead of its time since it lacked proper resolution techniques in observational astronomy. In 1963, Sjur Refsdal published a detailed analysis of properties of point mass gravitational lens, and advocated the application of geometrical optics to gravitational lensing effects (Refsdal, 1964).

Till then all the work done on gravitational lensing was just in theory. But when Walsh and Carswell observed an identical spectra of two nearby quasars, Weymann confirmed that these were gravitationally lensed images of a single quasar – Q0957 + 561 (Walsh et al., 1979). After the detection of this first gravitational lens system in 1979, the field of gravitational lensing boomed. The observation of multiple images of a source through gravitational lensing encodes a bunch of information about the source and the lens.

Motivation

Gravitational lensing encounters various observational challenges – multiple-imaging is a rare phenomenon, large magnification can disguise the nature of the source, the lens mass distribution is uncertain. In recent times a number of dedicated surveys have been conducted on gravitational lensing. Robust techniques are being used to measure time delays between lensed images. One of the application of time delay measurements is to obtain accurate value of the Hubble constant H_0 (Suyu et al., 2017).

Novel methods are being explored (Basu et al., 2020) to constrain the mass of axion-like particles (ALPs) which is a promising candidate of dark matter (Dine et al., 1981; Peccei and Quinn, 1977; Wilczek, 1978). This technique exploits the interaction between photons and ALPs which exhibits parity violation. This causes the left- and right-handed circularly polarized light to propagate at different velocities in the ALP field. This is the birefringence phenomenon. The polarization plane of linearly polarized light in the presence of ALP field is rotated. Thus multiple images of gravitationally lensed linearly polarized sources (like quasars) experiences different amounts of rotation. This rotation measure along with the time delay measurements between the images can provide stringent constraints on mass of ALPs dark matter.

The task of my thesis project is to study the range of possible time delays in gravitational lenses and to produce a catalogue of candidate lens systems which could be selected for follow up observations in order to further constrain or detect dark matter in the form of axion-like particles.

Chapter 2

Basic Concepts

In this chapter we take a brief look at the basic concepts and mathematical construction required for the development of this thesis. We restrict our discussion to topics relevant to understand the subsequent chapters. The chapter is divided into two sections. The first section introduces cosmic distances, cosmological model of the universe and the problem of dark matter. The second section deals with gravitational lensing.

2.1 Cosmology and the Problem of Dark Matter

Modern cosmology is founded on the framework of general relativity. Einstein's equation for general relativity describes the relation between spacetime curvature and energy-momentum tensor,

$$G_{\mu\nu} + \Lambda g_{\mu\nu} = 8\pi G T_{\mu\nu} \ , \tag{2.1}$$

where $G_{\mu\nu}$ is the Einstein tensor, $g_{\mu\nu}$ is the metric tensor, Λ is the cosmological constant, G is the Gravitational constant and $T_{\mu\nu}$ is the energy-momentum tensor. Note that natural units with $c \equiv 1$ is being used.

The Einstein tensor is defined as

$$G_{\mu\nu} \equiv R_{\mu\nu} - \frac{1}{2} R g_{\mu\nu} \ , \tag{2.2}$$

where $R_{\mu\nu}$ is the Ricci tensor and R is the Ricci scalar.

2.1.1 Robertson-Walker Metric

The cosmological principle states that our Universe is spatially homogeneous and isotropic. Homogeneity refers to the metric being the same throughout the manifold and isotropy states that the space looks the same in any direction. That is, homogeneity can be considered as invariance under translations and isotropy as invariance under rotations. These two assumptions give rise to a maximally symmetric space. To reconcile the cosmological principle with the observable Universe, we consider it evolving in time. Thus the spacetime metric can be written as

$$ds^2 = -dt^2 + a^2(t) \left[\frac{dr^2}{1 - kr^2} + r^2 (d\theta^2 + \sin^2 \theta d\phi^2) \right] \tag{2.3}$$

where r, θ, ϕ are the spatial coordinates, t is the time coordinate, $a(t)$ is the dimensionless time-varying scale factor and parameter $k = +1, 0, -1$ represents the curvature of the Universe. This is the Robertson-Walker (RW) metric.

2.1.2 Friedmann Equations

The Friedmann equations relate the scale factor $a(t)$ to the pressure p and density ρ of the universe. To arrive at these equations, we treat matter and energy as a perfect fluid, and insert the RW metric in the Einstein's equation.

$$Ist\ Friedmann\ Equation: \qquad \left(\frac{\dot{a}}{a}\right)^2 = \frac{8\pi G}{3}\rho - \frac{k}{a^2} + \frac{\Lambda}{3} \tag{2.4}$$

$$IInd\ Friedmann\ Equation: \qquad \frac{\ddot{a}}{a} = -\frac{4\pi G}{3}(\rho + 3p) + \frac{\Lambda}{3} \tag{2.5}$$

These equations define the Friedmann-Robertson-Walker (FRW) universe, also known as Friedmann-Lemaître-Robertson-Walker (FLRW) universe. The rate at which the scale factor increases characterizes the rate of expansion, and is defined as the Hubble parameter,

$$H(t) = \frac{\dot{a}(t)}{a(t)} \, . \tag{2.6}$$

The value of the Hubble parameter at the present epoch is the Hubble constant, $H_0 \equiv \dfrac{\dot{a}(t_0)}{a(t_0)}$. Recent measurements by the Planck Collaboration (Aghanim et al., 2020) quote it's value to be $H_0 = 67.4 \pm 0.5$ km/sec/Mpc.

In eq. (2.4), for $\Lambda = 0$ and $k = 0$, we obtain an expression for density which is known as the critical density,

$$\rho_{crit} = \frac{3H^2}{8\pi G} \, . \tag{2.7}$$

This quantity generally changes with time. It is seen from the Friedmann equation (2.4) that ρ_{crit} sets a limit on the sign of k, thus describing the geometry of the universe.

$$\begin{array}{lcll} \rho < \rho_{crit} & \Leftrightarrow & k < 0 & \Leftrightarrow \quad open\ universe \\ \rho = \rho_{crit} & \Leftrightarrow & k = 0 & \Leftrightarrow \quad flat\ universe \\ \rho > \rho_{crit} & \Leftrightarrow & k > 0 & \Leftrightarrow \quad closed\ universe \end{array}$$

A Friedmann model is uniquely determined by four parameters, known as the cosmological parameters,

$$H_0 = \frac{\dot{a}_0}{a_0} \, , \qquad \Omega_M = \frac{8\pi G}{3H_0^2}\rho \, , \qquad \Omega_\Lambda = \frac{\Lambda}{3H_0^2} \, , \qquad \Omega_k = -\frac{k}{a_0^2 H_0^2} \, , \tag{2.8}$$

where subscript 0 denotes the present time t_0. The Friedmann equation (2.4) can be rewritten in terms of the cosmological parameters as

$$\Omega_M + \Omega_\Lambda + \Omega_k = 1 \, . \tag{2.9}$$

Current observations and measurements (Aghanim et al., 2020) have set the values of

$$\Omega_M \sim 0.3 \, , \quad \Omega_\Lambda \sim 0.7 \, , \quad \Omega_k \sim 0 \, . \tag{2.10}$$

The accepted model of the present-day universe describes a spatially flat, expanding universe.

2.1.3 Redshifts and Distances

As the universe expands, the frequency ω_{em} of the emitted photon from a distant object at time t is observed with a lower frequency ω_{obs} at time t_0,

$$\frac{\omega_{obs}}{\omega_{em}} = \frac{a(t)}{a(t_0)} \, . \tag{2.11}$$

This is expressed in terms of redshift z between the two events which is defined as the fractional change in wavelength,

$$z_{em} = \frac{\lambda_{obs} - \lambda_{em}}{\lambda_{em}} \, , \tag{2.12}$$

or,

$$1 + z = \frac{a(t_0)}{a(t)} \, . \tag{2.13}$$

Thus, the redshift of an object can be used as a measure of its distance to us.

Measuring cosmic distances is non-trivial since the universe is expanding, and it is not directly measurable. There are different theory-based distances defined. It also depends on the cosmology of the universe, i.e., on the cosmological parameters. For simplicity, we choose $k = 0$ and matter-only ($\Omega_M = 1$) universe.
The proper distance D_{prop} is defined as the distance light propagates between two points. That is the proper distance between objects at redshifts z_1 and z_2 (with $z_1 < z_2$) is defined as the distance measured by the travel time of photon propagating from z_1 to z_2. It incorporates the expansion of the universe and is expressed as

$$\begin{aligned} D_{prop} &= c(t_1 - t_2) \\ \Rightarrow D_{prop} &= \frac{2c}{3H_0}[(1+z_1)^{-3/2} - (1+z_2)^{-3/2}] \, . \end{aligned} \tag{2.14}$$

The proper distance is closely related to the comoving distance D_{com}. It is defined as the distance which remains constant with epoch if the two objects are moving with the Hubble flow, i.e., the expansion of the universe. The comoving distance factors out the scale factor from the proper distance, i.e.,

$$D_{com} = \frac{2c}{3H_0}[(1+z_1)^{-1/2} - (1+z_2)^{-1/2}] \, . \tag{2.15}$$

The luminosity distance D_L is defined by the relation between the luminosity L of the source at z_2 and the flux F received at z_1,

$$D_L = \sqrt{\frac{L}{4\pi F}} \, . \tag{2.16}$$

The angular diameter distance D_A is the ratio of the objects physical size to its angular size. It also describes the distance between two objects at redshifts z_1 and z_2 as,

$$D_A = \frac{2c}{3H_0}\frac{1}{1+z_2}[(1+z_1)^{-1/2} - (1+z_2)^{-1/2}] \, . \tag{2.17}$$

The latter three distances can be expressed in terms of each other as,

$$D_{com} = (1+z_2)D_A \, , \tag{2.18}$$

$$D_L = \left(\frac{1+z_2}{1+z_1}\right)^2 D_A \, . \tag{2.19}$$

2.1.4 Missing Mass Problem

Brief History

Historically, "dark" matter was a term used often in astronomy to justify anomalies in calculations and corresponding observations. Generally, it represented matter that was too dim to be observed or the lack of precision equipment to observe it. Newton's laws of motion and universal gravitation enabled scientists to determine the gravitational mass of astronomical bodies by measuring their dynamical properties (Bertone and Hooper, 2018). A well-known example is the discovery of Neptune by studying the orbital motion of Uranus.
The Coma Cluster comprising of 800 galaxies exhibit a large velocity dispersion with respect to other clusters. To investigate the large scatter in the apparent velocities of eight galaxies within the Coma, Fritz Zwicky (in 1933) applied the virial theorem to determine the mass of the galaxy cluster. He found the velocity dispersion of 80 km/s whereas the observed average velocity dispersion along the line of sight was approximately 1000 km/s. This suggested mass discrepancy in the galaxy cluster. He concluded that the quantity of dark matter was much greater than luminous matter. Astronomers were skeptical of this result. At that time, it was believed that the dark matter was in the form of cool and cold stars, macroscopic and microscopic solid bodies, and gases.
Around 1970s, the galaxy rotation curves strongly suggested of missing mass in galaxies. The rotation curve of a galaxy is the rotational velocity profile of stars and gas about the center of the galaxy, given in km/s, plotted as a function of their distance from the Galactic center, usually given in kpc. The observed flat rotation curves at large galactocentric distances could be justified by the presence of large amounts of dark matter in the outer regions of galaxies. Eventually more evidence in support of the existence of dark matter was obtained.
The next question being asked was about the nature of dark matter. The discovery of cosmic microwave background (CMB) in 1965 refined the measurements of the primordial light element abundances. This set an upper limit on the cosmological baryon density, and suggested that the majority of dark matter was non-baryonic in nature. Today the accepted value of the density of dark matter is 84.4% of the total matter density (Zyla et al., 2020).
As the name suggests, dark matter do not interact much electromagnetically. Their influence is detected via gravitational effects. A number of subatomic particles are being considered to constitute dark matter. A few examples of dark matter candidates are neutrinos, WIMPs (weakly interacting massive particles), supersymmetric particles and axions. We take a closer look at axion-like dark matter particles.

ALPs Dark Matter

The theory of quantum chromodynamics (QCD) describes the strong forces acting between quarks and gluons very well. But the theory faces a problem, namely, the strong-CP problem. The QCD Lagrangian contains the term (Bertone and Hooper, 2018)

$$\mathcal{L}_{QCD} \supset \frac{\theta_{QCD}}{32\pi^2} g^2 G^{\alpha\mu\nu} \tilde{G}_{\alpha\mu\nu} \ , \tag{2.20}$$

where $G^{\alpha\mu\nu}$ is the gluon field strength tensor and θ_{QCD} is a quantity closely related to the phase of the QCD vacuum. The θ term is CP (charge-parity) violating and

gives rise to an electric dipole moment for the neutron

$$d_n \approx 3.6 \times 10^{-16} \theta_{QCD}\ e \text{ cm} , \tag{2.21}$$

where e is the charge on the electron. The (permanent, static) dipole moment is constraint to $|d_n| < 2.9 \times 10^{-26}\ e$ cm, implying

$$\theta_{QCD} \lesssim 10^{-10} . \tag{2.22}$$

This is a true fine tuning problem, since θ_{QCD} could obtain an $\mathcal{O}(1)$ contribution from the observed CP-violation in the electroweak sector, which must be cancelled to high precision by the (unrelated) gluon term (Marsh, 2016). This is the essence of the strong-CP problem.
A solution to this problem was proposed by Peccei and Quinn (in 1977). They showed that by introducing a new global $U(1)$ symmetry that is spontaneously broken, the quantity θ_{QCD} can be dynamically driven towards zero, naturally explaining the small observed value (Bertone and Hooper, 2018). Wilczek and Weinberg each independently pointed out that such a broken global symmetry also implies the existence of a Nambu-Goldstone boson called the axion. The axion acquires a small mass as a result of the $U(1)$ symmetry's chiral anomaly, on the order of $m_a \sim \lambda_{QCD}^2 / f_{PQ}$, where f_{PQ} is the scale at which the symmetry is broken and $\lambda_{QCD} \sim 200$ MeV is the scale of QCD.
The mass constraints on axions ($m_a \lesssim 10^{-3}$ eV) indicate that these particles are stable over cosmological time scales, and could constitute the dark matter.
Axions/ALPs are coupled to photons as (Carosi et al., 2013),

$$\mathcal{L} = -\frac{g_{\alpha\gamma}}{4} a F_{\mu\nu} \tilde{F^{\mu\nu}} = g_{\alpha\gamma} a \vec{E}.\vec{B} , \tag{2.23}$$

where $F_{\mu\nu}$ is the electromagnetic field tensor, a is the scalar field and $g_{\alpha\gamma}$ is the coupling constant of the photon and the scalar field.
In the presence of a magnetic field, the Primakoff interaction between axions and photons allows for the vacuum to become birefringent and dichroic (Marsh, 2016). These effects cause the polarization plane of linearly polarized light to be rotated as it propagates. This effect can be used to place constraints on the existence of axions.

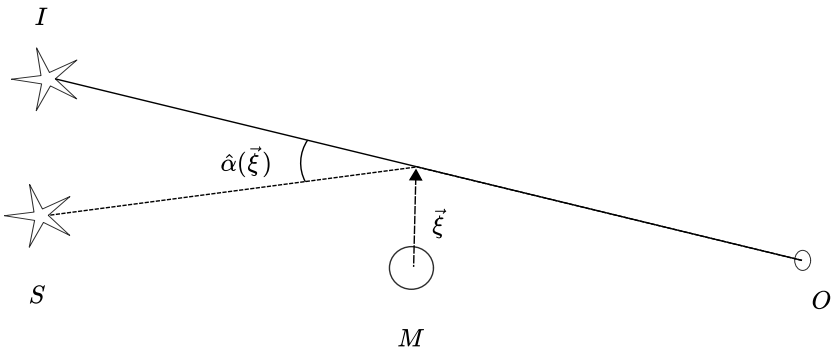

Figure 2.1: A sketch of a gravitational lens system. It shows the deflection angle $\hat{\alpha}(\vec{\xi})$ and the impact parameter or the minimum distance $\vec{\xi}$. M is the mass of the deflector (or lens), O is the observer and S is the source of a light ray. I is the image of the source S as observed by O.

2.2 Gravitational Lensing

The light rays coming from distant sources are influenced by the gravitational field of matter present between the source and the observer. This produces a slight displacement in the source position with respect to the case when there is no matter influence on the path of the light rays. This phenomenon is known as weak gravitational lensing. In some cases, the deflection due to a deflector (such as a galaxy, or cluster of galaxies) is strong enough to create multiple images of the background light source. This is termed as strong gravitational lensing. There are three distinct classes of multiple imaging – multiple images, arcs, and Einstein rings. Multiple images are often caused by a single quasar in the background of a galaxy producing double, triple or quadruple images. In this thesis, we will be focusing on strong gravitational lensing producing multiple images.

This section gives an overview of the basics of gravitational lensing. The concepts of deflection angle, lens geometry, multiple imaging, magnification ratio and time delay are covered here.

2.2.1 Deflection Angle

According to the theory of general relativity, light rays bend in the vicinity of massive objects. This bending of light rays gives rise to the apparent position of the light source (which we observe). A light ray which passes by a spherical body of mass M at a minimum distance ξ, is deflected by (Misner et al., 1973)

$$\frac{4GM}{c^2\xi} \ ,$$

where G is the gravitational constant and c is the speed of light.

For a 2-dimensional surface mass distribution, the mass term in the above equation can be expressed as $dM = \Sigma(\vec{\xi})d^2\xi$, where $\Sigma(\vec{\xi})$ is the surface mass density enclosed in area $d^2\xi$ (Figure 2.1) perpendicular to the sheet. In the jargon of gravitational lensing, this plane is known as the lens plane. The deflection angle for this case is,

$$\hat{\alpha}(\vec{\xi}) = \frac{4G}{c^2}\int_{\mathbb{R}^2} d^2\xi' \Sigma(\vec{\xi'})\frac{\vec{\xi}-\vec{\xi'}}{|\vec{\xi}-\vec{\xi'}|^2} \ , \tag{2.24}$$

where the integration is over the entire mass distribution in the lens plane .

For the validity of the above equations, two conditions must be satisfied: (i) weak gravitational fields must be considered, i.e., the deflection angle must be small, and (ii) stationary matter distribution of the deflector (lens), i.e., the velocity of the matter in the deflector (lens) must be much smaller than c (Schneider et al., 1999). Both the conditions are satisfied in astrophysical applications.

2.2.2 Lens Geometry and Lens Equation

Gravitational lensing can be explained based on the principles of geometrical optics. The lens equation relates the image position to the source position, and it can be easily derived from the geometry of the lens system (see Figure 2.2). The lens equation is

$$\vec{\beta} = \vec{\theta} - \frac{D_{ds}}{D_s}\hat{\alpha}(\vec{\xi}) \tag{2.25a}$$

or,

$$\vec{\beta} = \vec{\theta} - \vec{\alpha}(\vec{\theta}) \tag{2.25b}$$

where $\vec{\alpha}(\vec{\theta}) = \frac{D_{ds}}{D_s}\hat{\alpha}(\vec{\xi})$ is the scaled or reduced deflection angle. In terms of the displacement vectors $\vec{\eta}$ and $\vec{\xi}$, the lens equation is

$$\vec{\eta} = \frac{D_s}{D_d}\vec{\xi} - D_{ds}\hat{\alpha}(\vec{\xi}) \ . \tag{2.25c}$$

In the context of cosmology, the distances D's are the angular-diameter distances (2.17). The lens equation (2.25) may produce multiple images of a source at position $\vec{\eta}$ influenced by a particular mass distribution of the lens, i.e., for a given source position and mass distribution of the lens, a specific configuration of images is observed.

We may rewrite the lens equation in dimensionless form by scaling the variables as

$$\vec{x} = \frac{\vec{\xi}}{\xi_0} \ , \quad \vec{y} = \frac{\vec{\eta}}{\eta_0} \ , \tag{2.26}$$

where ξ_0 is an arbitrary length scale and $\eta_0 = \xi_0 \frac{D_s}{D_d}$.

Hence, the dimensionless lens equation is

$$\vec{y} = \vec{x} - \vec{\alpha}(\vec{x}) \tag{2.27}$$

where

$$\vec{\alpha}(\vec{x}) = \frac{1}{\pi}\int_{\mathbb{R}^2} d^2x' \kappa(\vec{x}') \frac{\vec{x} - \vec{x}'}{|\vec{x} - \vec{x}'|^2} = \frac{D_d D_{ds}}{\xi_0 D_s}\hat{\alpha}(\xi_0 \vec{x}) \tag{2.28}$$

is the scaled deflection angle, and

$$\kappa(\vec{x}) = \frac{\Sigma(\xi_0 \vec{x})}{\Sigma_{cr}} \tag{2.29}$$

denotes the dimensionless surface mass density. Σ_{cr} is the critical surface mass density defined as

$$\Sigma_{cr} = \frac{c^2 D_s}{4\pi G D_d D_{ds}} \ . \tag{2.30}$$

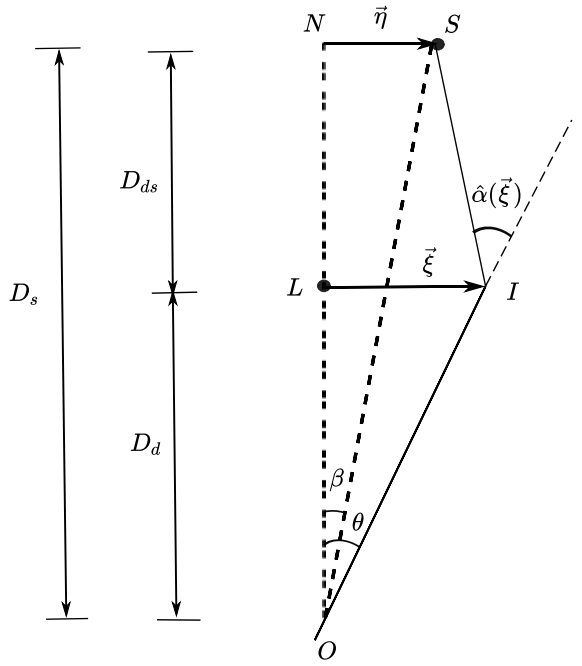

Figure 2.2: Geometry of gravitational lens system. S, L and O mark the positions of the source, lens (or deflector) and observer. Due to the bending of light rays near the vicinity of the lens L, the image I of the source is observed at an angular separation θ from the lens. The source S is at an angular separation β from the lens. D_d, D_{ds} and D_s are the distances between lens (or deflector) and observer, lens and source, and source and observer respectively. OLN is defined as the optical axis. The plane perpendicular to the optical axis and containing the lens is known as the lens plane. Similarly, the plane perpendicular to the optical axis and containing the source is known as the source plane.

The physical significance of critical surface mass density Σ_{cr} is that it provides the minimum value of surface mass density Σ required to produce multiple images of the background source.

A special case arises when the source is placed directly behind the lens, i.e., $\vec{\beta} = 0$, then due to rotational symmetry of the system, a ring-shaped image is observed. Such ring-shaped images are called "Einstein rings". The angular radius of this ring is called Einstein radius, and is defined as

$$\theta_E = \sqrt{\frac{4GM}{c^2}\frac{D_{ds}}{D_d D_s}} \, . \tag{2.31}$$

The deflection angle can also be expressed in terms of the gravitational potential $\psi(\vec{x})$ as

$$\vec{\alpha}(\vec{x}) = \nabla\psi(\vec{x}) \, , \tag{2.32}$$

where

$$\psi(\vec{x}) = \frac{1}{\pi}\int_{\mathbb{R}^2} d^2x' \kappa(\vec{x}\,') \ln|\vec{x} - \vec{x}\,'| \, . \tag{2.33}$$

Thus, the mapping $\vec{x} \mapsto \vec{y}$ is a gradient mapping,

$$\vec{y} = \nabla\left(\frac{1}{2}\vec{x}^2 - \psi(\vec{x})\right) \, , \tag{2.34}$$

or,

$$\nabla\phi(\vec{x},\vec{y}) = 0 \ , \tag{2.35}$$

where

$$\phi(\vec{x},\vec{y}) = \frac{1}{2}(\vec{x}-\vec{y})^2 - \psi(\vec{x}) \tag{2.36}$$

is the Fermat potential.

The relation (2.33) can be inverted, using the identity $\Delta \ln|\vec{x}| = 2\pi\delta^2(\vec{x})$, as

$$\Delta\psi = 2\kappa \ . \tag{2.37}$$

2.2.3 Magnification Factor

Magnification μ is defined as the ratio of the flux of an image to the flux of the corresponding unlensed source. Specific intensity or surface brightness is conserved (or constant) along any ray in empty space as a result of Liouville's theorem, and gravitational light deflection does not affect the spectral properties of the light rays, it only changes its direction and cross-section of a bundle of light rays. Thus, the surface brightness of the image is equal to that of the unlensed source. Therefore the magnification is simply the ratio of the solid angles subtended by the image $\Delta\omega$ to that of the unlensed source $(\Delta\omega)_0$.

$$\mu = \frac{\Delta\omega}{(\Delta\omega)_0} \ . \tag{2.38}$$

The ratio of the two solid angles is determined by the area-distortion of the lens mapping $\vec{\theta} \to \vec{\beta}$ given by the determinant of the Jacobian matrix,

$$\frac{(\Delta\omega)_0}{\Delta\omega} = \left|\det\frac{\partial\vec{\beta}}{\partial\vec{\theta}}\right| \ . \tag{2.39}$$

Thus, the magnification factor is

$$\mu = \left|\det\frac{\partial\vec{\beta}}{\partial\vec{\theta}}\right|^{-1} \ . \tag{2.40}$$

In terms of the dimensionless vectors,

$$\mu(\vec{x}) = \frac{1}{\det A(\vec{x})} \tag{2.41}$$

where

$$A(\vec{x}) = \frac{\partial\vec{y}}{\partial\vec{x}} \quad , \quad A_{ij} = \frac{\partial y_i}{\partial x_j} \tag{2.42}$$

is the Jacobian matrix for the scaled lens equation (2.27).

From (2.34), (2.36) and (2.42), $A_{ij} = \phi_{ij} = \delta_{ij} - \psi_{ij}$, where $\phi_{ij} \equiv \dfrac{\partial^2\phi}{\partial x_i \partial x_j}$ and $\psi_{ij} \equiv \dfrac{\partial^2\psi}{\partial x_i \partial x_j}$. Using (2.37), the Jacobian matrix takes the form

$$A = \begin{pmatrix} 1-\kappa-\gamma_1 & -\gamma_2 \\ -\gamma_2 & 1-\kappa+\gamma_1 \end{pmatrix} \tag{2.43}$$

where $\gamma_1 = \frac{1}{2}(\psi_{11} - \psi_{22})$, $\gamma_2 = \psi_{12} = \psi_{21}$ and $\gamma = \sqrt{\gamma_1^2 + \gamma_2^2}$ is the shear, which depends on the mass distribution outside of the lens system, and measures the anisotropic stretching of the image (Blandford and Narayan, 1992). The parameter κ is also known as the convergence and measures the isotropic part of magnification. Thus,

$$\det A = (1 - \kappa)^2 - \gamma^2 \tag{2.44}$$

and

$$\mu = [(1 - \kappa)^2 - \gamma^2]^{-1} \, . \tag{2.45}$$

Magnification $\mu_{(i)}$ of an image i is not directly measurable, but the relative magnification $\mu_{(i)}/\mu_{(j)}$ between two images i , j can be measured when the images are resolved.
In the lens plane where the Jacobian determinant vanishes, i.e., the curves which satisfy $\det A = 0$ in (2.44) are called critical curves. These curves separate regions in the lens plane where the Jacobian determinant has opposite sign. The sign of the Jacobian determinant denotes the parity of images. Images with positive parity (or positive Jacobian determinant) are said to have the same orientation as the unperturbed image and images with negative parity (or negative Jacobian determinant) have inverted orientation. Critical curves mapped to the source plane using the lens equation are called caustics. The number of images in a lensing system is closely related to the source position and the caustics. For a given position of observer and lens, the number of images varies with the source position. When the source crosses a caustic, the number of images changes by two.

2.2.4 Time Delay

A gravitationally lensed system with two or more images of a source, in general, will have different light-travel-times along different light paths. This happens due to two reasons: (i) geometrical time delay, it takes light rays different amounts of time to reach the observer for different path lengths, and (ii) potential (or, Shapiro) time delay, due to the influence of the gravitational field potential of the deflector on the light ray. The difference between the arrival times of two images is called time delay. It can be measured when the source is variable.

The excess light travel time of an image at $\vec{x}$ from source to observer with respect to the undeflected ray is given by the function,

$$\begin{aligned} T(\vec{x}, \vec{y}) &= \frac{\xi_0^2}{c} \frac{D_s}{D_d D_{ds}} (1 + z_d) \phi(\vec{x}, \vec{y}) \\ &= \frac{\xi_0^2}{c} \frac{D_s}{D_d D_{ds}} (1 + z_d) \left(\frac{(\vec{x} - \vec{y})^2}{2} - \psi(\vec{x}) \right) \, , \end{aligned} \tag{2.46}$$

where z_d is the redshift of the deflector.

The quantity $T(\vec{x}, \vec{y})$ cannot be measured, but the relative time delay between two images, $\Delta t = T^{(1)} - T^{(2)}$, is measurable. The time delay for a gravitational lensing system is the only dimensional observable, and can provide the overall length scale of the system.

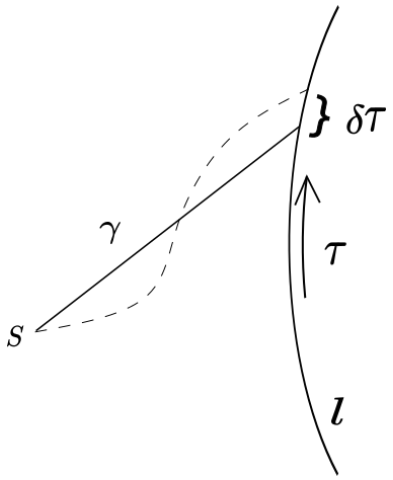

Figure 2.3: Geometry of Fermat's principle

Fermat's Principle

Light rays are characterized as null geodesics. In the study of gravitational lensing it is useful to exploit this property of light rays. As mentioned in the book "*Gravitational Lenses*" by P. Schneider, J. Ehlers, E.E. Falco, Fermat's principle states,

> "Let S be an event ('source') and l a time-like world line ('observer') in a spacetime $(M, g_{\alpha\beta})$. Then a smooth null curve γ from S to l is a light ray (null geodesic) if, and only if, its arrival time τ on l is stationary under first-order variations of γ within the set of smooth null curves from S to l (see Figure 2.3),
>
> $$\delta\tau = 0 \ ." \tag{2.47}$$

Let us explore Fermat's principle in two special cases.

Case I: Conformally stationary spacetime

A stationary spacetime is defined as spacetime whose geometry does not change with respect to time, i.e., it has a time-independent geometry. A special case of Fermat's principle concerning conformally stationary spacetimes, i.e., spacetimes whose physical metric $\tilde{ds}^2$ is conformal to a stationary (time-independent) metric ds^2:

$$\tilde{ds}^2 = \Omega^2 ds^2 \quad , \quad \Omega > 0 \ . \tag{2.48}$$

The line element of a stationary spacetime has the form,

$$ds^2 = e^{2U}(dt - w_i dx^i)^2 - e^{-2U} dl^2 \ , \tag{2.49}$$

$$dl^2 = \gamma_{ij} dx^i dx^j \ . \tag{2.50}$$

U, ω_i, γ_{ij} are functions of the spatial coordinates x^i only. ω_i is a 3-vector, called the twist vector, it represents rotation in the spacetime geometry. dl^2 is a spatial Riemannian (positive definite) metric. Ω is the conformal factor, it may depend on all four coordinates.

Null curves are invariant under conformal transformation. Thus curves which are

light like or light like geodesics w.r.t. $\tilde{ds}^2$ have the same properties also w.r.t. ds^2, one may apply Fermat's theorem to ds^2 to find the light rays of $\tilde{ds}^2$.

On a future-direction null curve,

$$ds^2 = 0 \, . \tag{2.51}$$

Applying (2.51) to (2.49), we get

$$dt = \omega_i dx^i + e^{-2U} dl \, . \tag{2.52}$$

On integrating over the null curve,

$$t = \int_{\tilde{\gamma}} (\omega_i dx^i + e^{-2U} dl) \, , \tag{2.53}$$

and applying Fermat's principle, we get

$$\delta \int_{\tilde{\gamma}} (\omega_i dx^i + e^{-2U} dl) = 0 \, , \tag{2.54}$$

where the spatial paths $\tilde{\gamma}$ are to be varied with fixed endpoints.

(2.54) is analogous to classical Fermat's principle if we define

$$n = e^{-2U} + \omega_i \frac{dx^i}{dl} \tag{2.55}$$

as (position and direction dependent) effective index of refraction. dl represents the geometrical arc length.

Case II: Conformally static spacetime

A further special case of stationary spacetime is the static spacetime in which $\omega_i = 0$, i.e., the spacetime has a time-independent and irrotational geometry. In this case, the vacuum behaves like an isotropic, non-dispersive medium with index,

$$n = e^{-2U} \, . \tag{2.56}$$

Hence for (conformally) stationary spacetime, Fermat's principle can also be stated as [see (2.54)], "the spatial paths of light rays are geodesics w.r.t. the Finsler metric $\omega_i dx^i + e^{-2U} dl$, which is Riemannian if $\omega_i = 0$."

The approximate metric of isolated, slowly moving, non-compact matter distributions can be expressed as the Schwarzschild metric,

$$\begin{aligned} ds^2 &= g_{\alpha\beta} dx^\alpha dx^\beta \, , \\ ds^2 &\approx \left(1 + \frac{2U}{c^2}\right) c^2 dt^2 - \left(1 - \frac{2U}{c^2}\right) d\vec{x}^2 \, . \end{aligned} \tag{2.57}$$

Arrival time and Fermat potential

Fermat's principle is the principle of stationary arrival time. In other words, light rays minimize the arrival time. To get some analytical insight, we consider a system with the following assumptions:

(i) An isolated system of a (point) source, the deflecting mass distribution and the observer.

(ii) Geometrically thin lens and small deflection.

According to metric (2.57), for the null geodesic

$$t = c^{-1} \int \left(1 - \frac{2U}{c^2}\right) dl = c^{-1} l - 2c^{-3} \int U dl \tag{2.58}$$

where l is the Euclidean length of the path SIO [see Figure (2.2)], and can be written as

$$\begin{aligned} l &= \sqrt{(\vec{\xi} - \vec{\eta})^2 + D_{ds}^2} + \sqrt{\vec{\xi}^2 + D_d^2} \\ &\approx D_{ds} + D_d + \frac{1}{2D_{ds}}(\vec{\xi} - \vec{\eta})^2 + \frac{1}{2D_d}\vec{\xi}^2 \end{aligned} \tag{2.59}$$

where $\vec{\eta}$ is the position of the source perpendicular to the optical axis OL (L is the center of the lens and O is the observer) and $\vec{\xi}$ is the perpendicular position of the image from the optical axis. D_d, D_s, D_{ds} refer to Euclidean background metric.

And U is the Newtonian potential expressed as,

$$U(t, \vec{x}) := -G \int \frac{\rho(t, \vec{x} + \vec{y})}{|\vec{y}|} d^3y \ . \tag{2.60}$$

In case of Schwarzschild lens with point mass potential,

$$U = -\frac{GM}{r} \ . \tag{2.61}$$

To further evaluate eq.(2.58), we first integrate the potential U of a point mass from S to I,

$$\int_S^I U dl = GM \left[\ln \frac{|\vec{\xi}|}{2D_{ds}} + \frac{\vec{\xi} \cdot (\vec{\eta} - \vec{\xi})}{|\vec{\xi}| D_{ds}} + \mathcal{O}\left(\left(\frac{\vec{\eta} - \vec{\xi}}{D_{ds}}\right)^2\right)\right] \ . \tag{2.62}$$

Under the conditions of lensing, this can be approximated by

$$\int_S^I U dl = GM \ln \frac{|\vec{\xi}|}{2D_{ds}} \ . \tag{2.63}$$

Consider an arbitrary length scale ξ_0 such that $\xi_0 < D_{ds}$ and $|\vec{\xi}| < \xi_0$, then (2.63) can be decomposed as,

$$\int_S^I U dl = GM \left(\ln \frac{|\vec{\xi}|}{2\xi_0} + \ln \frac{\xi_0}{D_{ds}} \right) \ . \tag{2.64}$$

The first term on the right is due to the ray contained in a slab of thickness ξ_0 above the lens plane and the second term is due to the ray outside this slab.

Similarly, we obtain the integral for ray from I to O. On adding both parts, we get the expression for the potential time delay as

$$\frac{-2}{c^3}\int U dl = \frac{-4G}{c^3}\int d^2\xi' \Sigma(\vec{\xi'}) \ln\left(\frac{|\vec{\xi}-\vec{\xi'}|}{\xi_0}\right) + \text{const.} \tag{2.65}$$

The first term in the right describes a "local" effect which arises in a neighbourhood of the lens.
Next, we add the geometrical and potential contributions to the arrival time and subtract the - purely geometrical - arrival time for an unlensed ray from S to O. This gives the time delay of a kinematically possible ray relative to the undeflected ray,

$$c\Delta t = \hat{\phi}(\vec{\xi}, \vec{\eta}) + \text{const.} \tag{2.66}$$

where,

$$\hat{\phi}(\vec{\xi}, \vec{\eta}) = \frac{D_d D_s}{2D_{ds}}\left(\frac{\vec{\xi}}{D_d} - \frac{\vec{\eta}}{D_s}\right)^2 - \hat{\psi}(\vec{\xi}) \tag{2.67}$$

is the Fermat potential,

$$\hat{\psi}(\vec{\xi}) = \frac{4G}{c^2}\int d^2\xi' \Sigma(\vec{\xi'}) \ln\left(\frac{|\vec{\xi}-\vec{\xi'}|}{\xi_0}\right) \tag{2.68}$$

is the deflection potential and const. is independent of $\vec{\xi}$ and $\vec{\eta}$.
Now, we apply Fermat's principle to (2.66),

$$\frac{\partial(\Delta t)}{\partial\vec{\xi}} = 0$$

$$\Rightarrow \vec{\eta} = \frac{D_s}{D_d}\vec{\xi} - D_{ds}\hat{\alpha}(\vec{\xi}) \; . \tag{2.69}$$

This is the lens mapping equation, or the lens equation. It relates source and image positions, for a given deflecting mass.
Here,

$$\hat{\alpha}(\vec{\xi}) = \nabla\hat{\psi} \tag{2.70}$$

is the deflection angle.
In terms of the Fermat potential, the lens equation can be written as,

$$\nabla_{\vec{\xi}}\,\hat{\phi}(\vec{\xi}, \vec{\eta}) = 0 \; . \tag{2.71}$$

From (2.66), the arrival time difference (or time delay) for two images $\vec{\xi}^{(1)}$, $\vec{\xi}^{(2)}$ of a source at position $\vec{\eta}$ can be expressed as,

$$c(t_1 - t_2) = \hat{\phi}(\vec{\xi}^{(1)}, \vec{\eta}) - \hat{\phi}(\vec{\xi}^{(2)}, \vec{\eta}) \tag{2.72}$$

where $(t_1 - t_2)$ is the difference of the coordinate times at which the light rays arrive at the observer.

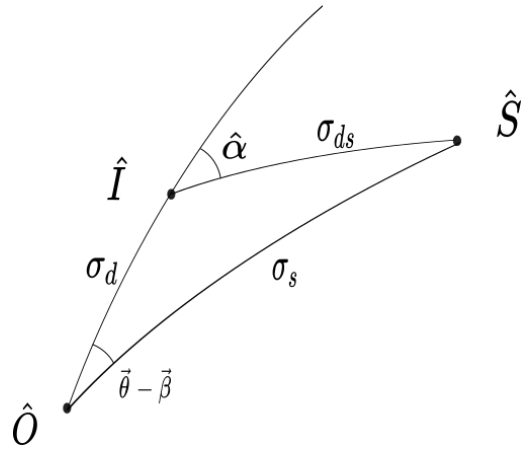

Figure 2.4: The events S, I, O are projected into the comoving 3-space Σ_k of constant curvature k. The rays form a geodesic triangle $\hat{S}\hat{I}\hat{O}$ in Σ_k.

Substituting the equations of $\hat{\phi}$ from (2.67) in (2.72), we get

$$c(t_1 - t_2) = \frac{D_d D_s}{2D_{ds}} \left[\left(\frac{\vec{\xi}^{(1)}}{D_d} - \frac{\vec{\eta}}{D_s} \right)^2 - \left(\frac{\vec{\xi}^{(2)}}{D_d} - \frac{\vec{\eta}}{D_s} \right)^2 \right] + \frac{4G}{c^2} \int d^2\xi' \Sigma(\vec{\xi}') \ln \left(\frac{|\vec{\xi}^{(2)} - \vec{\xi}'|}{|\vec{\xi}^{(1)} - \vec{\xi}'|} \right) . \quad (2.73)$$

On substituting the lens equation (2.69), we can rewrite the above equation as

$$c(t_1 - t_2) = \frac{D_d D_{ds}}{2D_s} \left[(\hat{\alpha}(\vec{\xi}^{(1)}))^2 - (\hat{\alpha}(\vec{\xi}^{(2)}))^2 \right] + \frac{4G}{c^2} \int d^2\xi' \Sigma(\vec{\xi}') \ln \left(\frac{|\vec{\xi}^{(2)} - \vec{\xi}'|}{|\vec{\xi}^{(1)} - \vec{\xi}'|} \right) . \quad (2.74)$$

We can also rewrite eq. (2.73) in terms of the dimensionless vectors

$$(t_1 - t_2) = \frac{\xi_0^2}{c} \frac{D_s}{D_d D_{ds}} \left[\frac{(\vec{x}^{(1)} - \vec{y})^2}{2} - \frac{(\vec{x}^{(2)} - \vec{y})^2}{2} - \psi(\vec{x}^{(1)}) + \psi(\vec{x}^{(2)}) \right] . \quad (2.75)$$

This expression of time delay is obtained in an asymtotically flat spacetime. We now consider it in the cosmological context.

We can write the Robertson-Walker (RW) metric as

$$ds^2 = a^2(\eta)[d\eta^2 - d\sigma^2] \quad (2.76)$$

where $\eta := c \int \frac{dt}{a(t)}$ is the conformal time and $d\sigma^2 = \frac{d\vec{x}^2}{(1 + \frac{k}{4}\vec{x}^2)^2}$ is the metric of the 3-dimensional simply-connected Riemannian space of constant curvature $k = 1, 0$ or -1.

For null geodesics, $ds^2 = 0$, then according to the RW metric (2.76), the geometrical time delay is given as

$$\Delta\eta_{geom} = \sigma_{ds} + \sigma_d - \sigma_s \quad (2.77)$$

where σ's denote distances measured by the metric $d\sigma^2$.
Since the time delay is very small compared to the Hubble time H_0^{-1}, we can write

$$c\Delta t_{geom} = a_0 \Delta\eta_{geom} \ . \tag{2.78}$$

By considering the geometry of the system (see Fig. 2.4) and (2.77), we get

$$\Delta\eta_{geom} = \frac{\sin\sigma_{ds}\sin\sigma_d}{2\sin\sigma_s}\ \hat{\alpha}^2 \ . \tag{2.79}$$

The relation between σ-distances and angular diameter distances can be easily obtained by recalling that conformal transformation preserves angles,

$$D_{ds} = a_s \sin\sigma_{ds} \ , \tag{2.80}$$
$$D_d = a_d \sin\sigma_d \ , \tag{2.81}$$
$$D_s = a_s \sin\sigma_s \ . \tag{2.82}$$

Fig. 2.4 shows that $(\vec{\theta}-\vec{\beta})\sin\sigma_s = \hat{\alpha}\sin\sigma_{ds}$. Substituting these equations in (2.77) and (2.78), and recalling that $\dfrac{a_0}{a_d} = 1+z_d$ gives

$$c\Delta t_{geom} = (1+z_d)\frac{D_d D_s}{2D_{ds}}(\vec{\theta}-\vec{\beta})^2 \ . \tag{2.83}$$

The $\vec{\xi}$-dependent part of the potential time delay arises locally when a ray traverses the neighbourhood of the lens. Thus, the cosmological potential time delay is obtained by introducing the redshift to the local one,

$$c\Delta t_{pot} = -(1+z_d)\hat{\psi}(\vec{\xi}) + \text{const.} \tag{2.84}$$

where the constant is the same for all rays from the source to the observer.

The total time delay of the deflected ray to the unperturbed ray is given as

$$c\Delta t = (1+z_d)\left(\frac{D_d D_s}{2D_{ds}}(\vec{\theta}-\vec{\beta})^2 - \hat{\psi}(\vec{\xi})\right) + \text{const.} \ . \tag{2.85}$$

Chapter 3

Lens Models in Asymptotically Flat Spacetime

Now we take a closer look at particular models of gravitational lensing systems with different degrees of symmetry. It is easier to analyse and understand the physics of systems with maximal symmetry, so we start our analysis from there, and progress to systems which are less symmetric.

A lensing system describes the gravitational potential of the lensing object and the configuration of the images produced. Depending on the positions of source and lens, the properties of images of the system change.

3.1 Schwarzschild Lens

A point-mass lens or Schwarzschild lens is the simplest case due to it's spherical symmetry. The entire lens mass is localized at a point. In reality this is never the case (except for black holes, but we are not considering that), but systems with large ratio of Einstein's radius θ_E to angular diameter size of the lens can be well approximated by it.

The deflection angle is given as [from (2.24)],

$$\hat{\alpha}(\vec{\xi}) = \frac{4GM}{c^2|\vec{\xi}|}\hat{\xi}\ , \tag{3.1}$$

and the lens equation is [from (2.25)],

$$\begin{aligned} \vec{\beta} &= \vec{\theta} - \frac{D_{ds}}{D_s}\frac{4GM}{c^2|\vec{\xi}|}\hat{\xi} \\ &= \theta\hat{\xi} - \frac{D_{ds}}{D_s}\frac{4GM}{c^2}\frac{1}{\theta D_d}\hat{\xi}\ . \end{aligned} \tag{3.2}$$

A one-dimensional analysis is enough to describe this situation and two images are observed.

$$\beta = \theta - \frac{\theta_E^2}{\theta} \quad \Rightarrow \theta^2 - \beta\theta - \theta_E^2 = 0\ . \tag{3.3}$$

On solving the above quadratic equation, we get

$$\theta_\pm = \frac{\beta \pm \sqrt{4\theta_E^2 + \beta^2}}{2}\ . \tag{3.4}$$

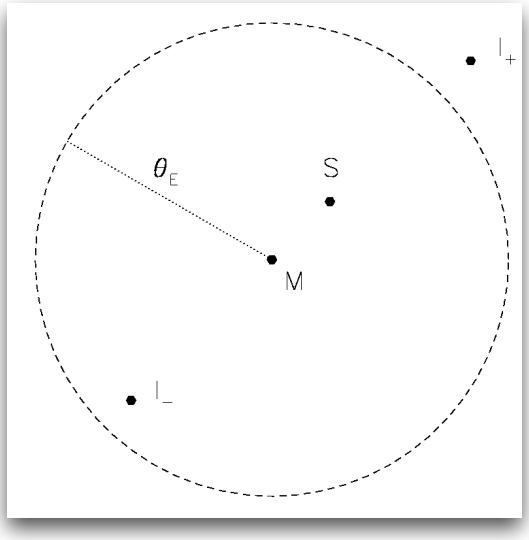

Figure 3.1: A schematic representation showing the positions of the source S and the two images I_-, I_+, the lens M and the Einstein's radius θ_E (Meneghetti, 2019).

Thus, the images are formed on either side of the source, i.e., the lens, source and both images lie on the same plane. But for the case when the source is right behind the lens, i.e., $\vec{\beta} = 0$, then since there is no preferred direction a ring-shaped image is observed, called the Einstein ring, with angular radius θ_E (Figure 3.1).

Let us define normalized angles as

$$\tilde{\theta} = \frac{\theta}{\theta_E} \,, \quad \tilde{\beta} = \frac{\beta}{\theta_E} \,. \tag{3.5}$$

From (3.4), we get

$$\tilde{\theta}_\pm \;\; = \;\; \frac{1}{2}(\tilde{\beta} \pm \sqrt{4 + \tilde{\beta}^2}) \,. \tag{3.6}$$

Magnification is given as the ratio of the solid angle subtended by the image to the solid angle subtended by the source. The surface area of the (infinitesimal) source perpendicular to the plane of Fig. 2.2 is $D_s \Delta\tilde{\beta}\; D_s\tilde{\beta}\Delta\hat{\phi}$ where $\Delta\hat{\phi}$ is the angular size perpendicular to the optical axis. Thus, the (normalized) solid angle of the source $(\Delta\omega)_0$ is given as $\Delta\tilde{\beta}\;\tilde{\beta}\Delta\hat{\phi}$. Similarly, the (normalized) solid angle of the image $\Delta\omega$ is $\Delta\tilde{\theta}\;\tilde{\theta}\Delta\hat{\phi}$. $\Delta\hat{\phi}$ remains the same for both due to the symmetry of the lens. From (2.38), the absolute values of the magnification factors of the images $(i = +, -)$ are

$$\mu_\pm = \left| \frac{\Delta\tilde{\theta}_i \;\tilde{\theta}_i}{\Delta\tilde{\beta}\;\tilde{\beta}} \right| \,. \tag{3.7}$$

From (3.6), we find

$$\mu_\pm = \frac{1}{4}\left(\frac{\tilde{\beta}}{\sqrt{\tilde{\beta}^2 + 4}} + \frac{\sqrt{\tilde{\beta}^2 + 4}}{\tilde{\beta}} \pm 2 \right) \,, \tag{3.8}$$

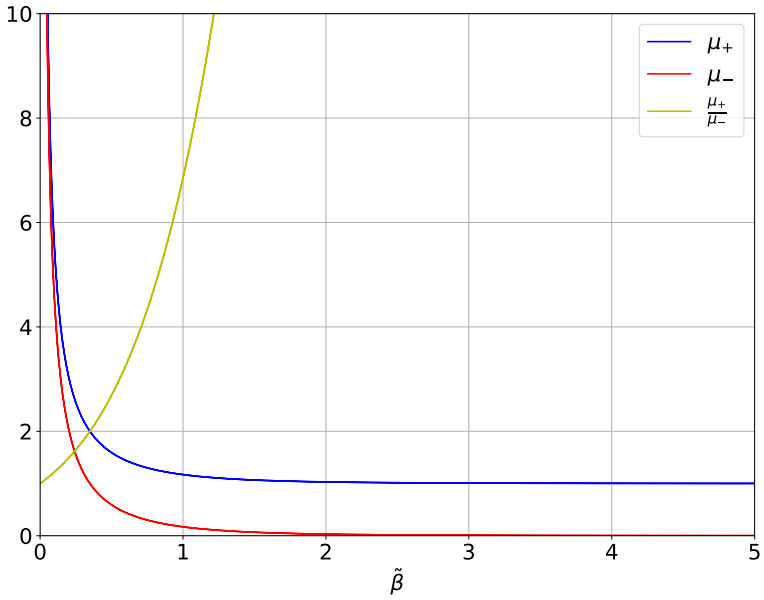

Figure 3.2: Magnifications of the two images is plotted with respect to $\tilde{\beta}$ (blue and red solid curves) and the magnification ratio of the images is represented by the yellow curve.

where $\tilde{\beta} \geq 0$.

The flux ratio (magnification ratio) is

$$\frac{\mu_+}{\mu_-} = \left[\frac{\sqrt{\tilde{\beta}^2+4}+\tilde{\beta}}{\sqrt{\tilde{\beta}^2+4}-\tilde{\beta}}\right]^2 \tag{3.9}$$

From the plot of the magnification ratio of the images (Figure 3.2), one can infer the source position ($\tilde{\beta} = \beta/\theta_E$) in terms of Einstein's radius. Using the lens equation, one can further solve for Einstein's radius, and once the distances of the lens system are known, the mass of the lens can be determined.

The deflection angle (3.1) together with the surface mass density of Schwarzschild lens

$$\Sigma(\vec{\xi}) = M\delta_{2D}(\vec{\xi}) \tag{3.10}$$

can be used to further simplify the expression for time delay (2.74)

$$c(t_+ - t_-) = \frac{D_d D_{ds}}{2D_s}\left(\frac{4GM}{c^2}\right)^2\left[\left(\frac{1}{|\vec{\xi}_+|}\right)^2 - \left(\frac{1}{|\vec{\xi}_-|}\right)^2\right] + \frac{4GM}{c^2}\ln\left|\frac{\vec{\xi}_-}{\vec{\xi}_+}\right| . \tag{3.11}$$

This can be rewritten in terms of angular separation as

$$c(t_+ - t_-) = \frac{D_{ds}}{2D_d D_s}\left(\frac{4GM}{c^2}\right)^2\left[\left(\frac{1}{\theta_+}\right)^2 - \left(\frac{1}{\theta_-}\right)^2\right] + \frac{4GM}{c^2}\ln\left|\frac{\theta_-}{\theta_+}\right| \tag{3.12}$$

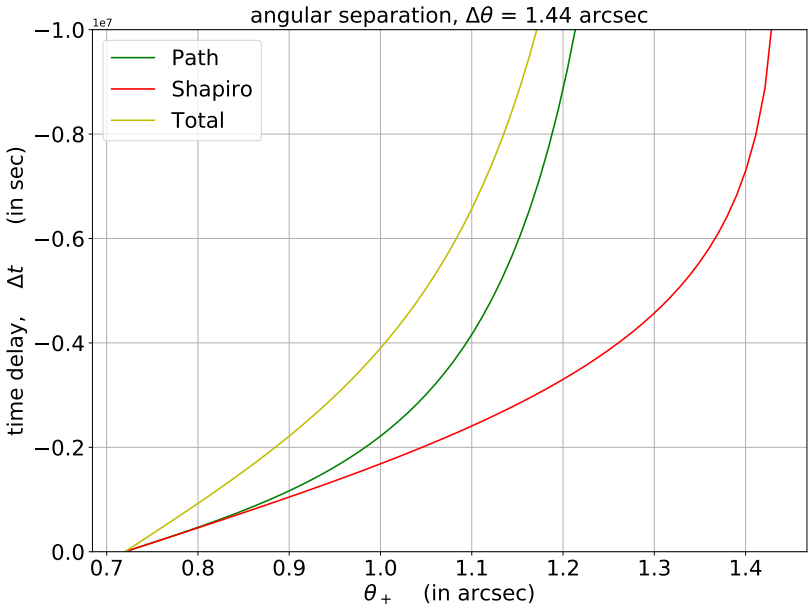

Figure 3.3: The variation of time delay between the two images with respect to the angular position θ_+ of I_+ is shown. Time delay due to Shapiro effect (red curve) and the path difference (green curve) are also plotted separately along with the total time delay (yellow curve).

or,

$$\frac{c(t_+ - t_-)}{R_S} = \left[\left(\frac{\theta_E}{\theta_+}\right)^2 - \left(\frac{\theta_E}{\theta_-}\right)^2\right] + 2\ln\left|\frac{\theta_-}{\theta_+}\right| \tag{3.13}$$

where θ_E is the (dimensionless) Einstein radius (2.31) and R_S is the Schwarzschild radius

$$R_S = \frac{2GM}{c^2} \,. \tag{3.14}$$

The dependence of time delay $(t_+ - t_-)$ on the image position of I_+ is seen in Fig. 3.3. The angular separation between the two images I_+ and I_- is $1.44''$. The negative time delay simply means that the arrival time of image at I_+ is less than that of image at I_-.

3.2 Axially Symmetric Lens

For a circularly-symmetric surface mass density, $\Sigma(\vec{\xi}) = \Sigma(|\vec{\xi}|)$. The ray-trace equation reduces to a one-dimensional form, since all light rays from the (point) source to the observer must lie in the plane spanned by the center of the lens, the source, and the observer. If the source, observer, and lens center are colinear, rays are not restricted to a single plane, and ring images can be formed.

The scaled deflection angle is given as,

$$\vec{\alpha}(\vec{x}) = \frac{1}{\pi}\int_{\mathbb{R}^2} d^2x' \kappa(\vec{x'}) \frac{\vec{x} - \vec{x'}}{|\vec{x} - \vec{x'}|^2} \,. \tag{3.15}$$

If we choose the impact vector $\vec{x}$ in the lens plane as $\vec{x} = (x, 0)$, $x \geq 0$. Then in polar coordinates, $\vec{x'} = x'(\cos\varphi, \sin\varphi)$ and $d^2x' = x'dx'd\varphi$. For symmetric matter distribution, $\kappa(\vec{x'}) = \kappa(x')$.

So, the components of the deflection angle can be written as,

$$\alpha_1(x) = \frac{1}{\pi}\int_0^\infty x'dx'\kappa(x')\int_0^{2\pi} d\varphi \frac{x - x'\cos\varphi}{x^2 + x'^2 - 2xx'\cos\varphi}\ , \tag{3.16}$$

$$\alpha_2(x) = \frac{1}{\pi}\int_0^\infty x'dx'\kappa(x')\int_0^{2\pi} d\varphi \frac{-x'\sin\varphi}{x^2 + x'^2 - 2xx'\cos\varphi}\ . \tag{3.17}$$

By symmetry, the second component $\alpha_2(x)$ vanishes, hence $\vec{\alpha} \mid\mid \vec{x}$.

Using the lens equation, $\vec{y} = \vec{x} - \vec{\alpha}(\vec{x})$, it is clear that the source position vector $\vec{y}$ must also be parallel to $\vec{x}$. Thus, the source, image, lens center and the observer, all lie in the same plane.

For the first component $\alpha_1(x)$, if $x' > x$, the inner integral vanishes and, if $x' < x$, then it is equal to $2\pi/x$. Thus, only the matter within the disc of radius x around the center of mass contributes to the deflection at the point $\vec{x}$ as if it were located at that center, and the matter outside does not contribute. Hence, we have

$$\alpha(x) \equiv \alpha_1(x) = \frac{1}{x}\, 2\int_0^x x'dx'\kappa(x') \equiv \frac{m(x)}{x} \tag{3.18}$$

where $m(x)$ defines the dimensionless mass within a circle of radius x.

The relation between the scaled deflection angle $\vec{\alpha}$ and the true deflection $\hat{\alpha}$ is

$$\hat{\alpha}(\vec{\xi}) = \frac{\xi_0 D_s}{D_d D_{ds}}\ \vec{\alpha}(\vec{\xi}/\xi_0) \tag{3.19}$$

where ξ_0 is an arbitrary length scale in the lens plane. Thus, for a circularly-symmetric mass distribution,

$$\begin{aligned}
\hat{\alpha}(\xi) &= \frac{\xi_0 D_s}{D_d D_{ds}}\ \alpha(x) \\
&= \frac{\xi_0 D_s}{D_d D_{ds}}\frac{\xi_0}{\xi}\, 2\int_0^\xi \frac{\xi'}{\xi_0}\frac{d\xi'}{\xi_0}\frac{\Sigma(\xi')}{\Sigma_{cr}} \\
&= \frac{1}{\xi}\frac{4G}{c^2}\, 2\pi\int_0^\xi \xi' d\xi'\Sigma(\xi') \\
&\equiv \frac{4GM(\xi)}{c^2\xi}
\end{aligned} \tag{3.20}$$

where $\Sigma_{cr} = \dfrac{c^2}{4\pi G}\ \dfrac{D_s}{D_d D_{ds}}$ is the critical density and $M(\xi) = 2\pi\displaystyle\int_0^\xi \xi' d\xi'\Sigma(\xi')$ is the mass enclosed by the circle of radius ξ.

Hence, the scaled lens equation for circularly-symmetric matter distributions $\kappa = \kappa(|\vec{x}|)$, is

$$y = x - \alpha(x) = x - \frac{m(x)}{x} \tag{3.21}$$

where the range of x is taken to be the whole real axis, and $m(x) \equiv m(|x|)$.

Owing to symmetry, we can restrict our attention to source positions $y \geq 0$. Since $m(x) \geq 0$, any positive solution x of (3.21) must have $x \geq y$, and any negative one must obey $\dfrac{m(x)}{-x} > y$.

Consider the deflection angle at a point $\vec{x} = (x_1, x_2)$,

$$\vec{\alpha}(\vec{x}) = \frac{m(x)}{x^2}\vec{x} \tag{3.22}$$

where $x = |\vec{x}|$.
The Jacobian matrix is obtained as,

$$A = \mathcal{I} - \frac{m(x)}{x^4}\begin{pmatrix} x_2^2 - x_1^2 & -2x_1x_2 \\ -2x_1x_2 & x_1^2 - x_2^2 \end{pmatrix} - \frac{dm(x)}{dx}\frac{1}{x^3}\begin{pmatrix} x_1^2 & x_1x_2 \\ x_1x_2 & x_2^2 \end{pmatrix} \tag{3.23}$$

where $\mathcal{I}$ is the 2-D identity matrix and $\dfrac{dm}{dx} = 2x\kappa(x)$, i.e., the convergence is,

$$\kappa(x) = \frac{1}{2x}\frac{dm(x)}{dx} \ . \tag{3.24}$$

The components of shear are

$$\gamma_1(x) = \frac{1}{2}(x_2^2 - x_1^2)\left(\frac{2m}{x^4} - \frac{m'}{x^3}\right) \ , \tag{3.25}$$

$$\gamma_2(x) = x_1x_2\left(\frac{m'}{x^3} - \frac{2m}{x^4}\right) \ , \tag{3.26}$$

where $m' = \dfrac{dm}{dx}$. And,

$$\gamma(x) = \frac{m(x)}{x^2} - \kappa(x) \ . \tag{3.27}$$

The Jacobian determinant is

$$\det A = (1-\kappa)^2 - \gamma^2 \tag{3.28}$$

$$= (1-\kappa)^2 - \left(\frac{m}{x^2} - \kappa\right)^2 \tag{3.29}$$

$$= \left(1 - \kappa + \frac{m}{x^2} - \kappa\right)\left(1 - \kappa - \frac{m}{x^2} + \kappa\right) \tag{3.30}$$

$$= \left(1 - \frac{m}{x^2}\right)\left(1 + \frac{m}{x^2} - 2\kappa\right) \tag{3.31}$$

$$= \left(1 - \frac{\alpha(x)}{x}\right)\left(1 - \frac{d\alpha(x)}{dx}\right) \ . \tag{3.32}$$

The deflection potential (2.33) for this case can be solved as (consider $x \geq 0$),

$$\psi(x) = \frac{1}{\pi}\int_0^\infty dx' x' \kappa(x') \int_0^{2\pi} d\varphi \ln\sqrt{x^2 + x'^2 - 2xx'\cos\varphi} \ . \tag{3.33}$$

These integrals can be calculated using equation (4.224.14) of (Gradshteyn and Ryzhik, 2007),

$$\psi(x) = 2\ln x \int_0^x x'dx'\kappa(x') + 2\int_x^\infty x'dx'\kappa(x')\ln x' \ . \tag{3.34}$$

Since ψ is determined only upto an additive constant (Schneider et al., 1999), we can add the term

$$-2\int_0^\infty x'dx'\kappa(x')\ln x' \tag{3.35}$$

to (3.34), which then becomes

$$\psi(x) = 2\int_0^x x'dx'\kappa(x')\ln\left(\frac{x}{x'}\right) \ . \tag{3.36}$$

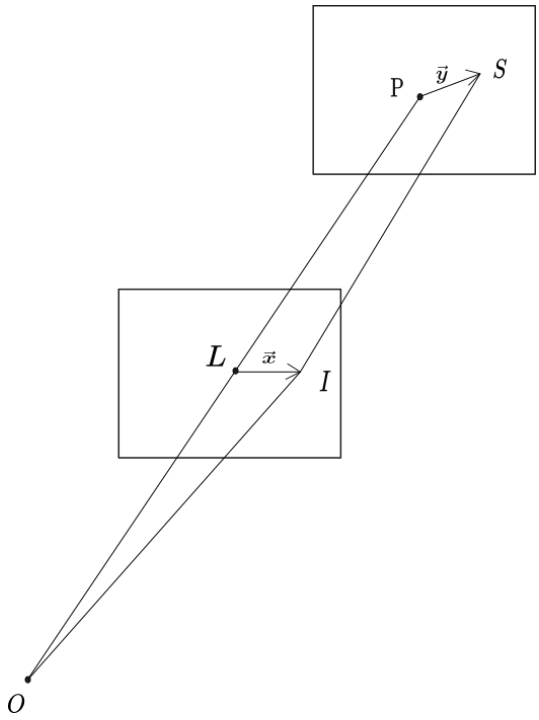

Figure 3.4: Geometry with scaled position vectors. Observer is at O, image is at I and the source is at S. OLP is the optical axis.

3.3 Perturbed Symmetric Lens

In reality, purely axi-symmetric lenses do not exist, but considering perturbed axially symmetric lenses approximate well with observations. An axially symmetric lens with perturbations due to large scale gravitational field can be approximated by its quadratic Taylor expansion – quadrupole terms – about the center of the main deflector.

The deflection caused by the perturber is

$$\vec{\alpha}_p(\vec{x}) = \vec{\alpha}_p(0) + \begin{pmatrix} \Gamma_1 & 0 \\ 0 & \Gamma_2 \end{pmatrix} \vec{x} \, . \tag{3.37}$$

From the equation of Jacobian matrix (2.43), $(\Gamma_1 + \Gamma_2)/2$ is the local surface mass density of the perturber κ_p, and $(\Gamma_1 - \Gamma_2)/2$ is its shear γ_p.

$$\Rightarrow \vec{\alpha}_p(\vec{x}) = \vec{\alpha}_p(0) + \begin{pmatrix} \kappa_p + \gamma_p & 0 \\ 0 & \kappa_p - \gamma_p \end{pmatrix} \vec{x} \tag{3.38}$$

Assume $\Gamma_1 \neq \Gamma_2$, since $\Gamma_1 = \Gamma_2$ results in a symmetric lens condition. The lens equation is

$$\vec{y} = \vec{x} - \vec{\alpha}(\vec{x}) \tag{3.39}$$

$$= \vec{x} - \bar{\kappa}(x)\vec{x} - \vec{\alpha}_p(0) - \begin{pmatrix} \Gamma_1 & 0 \\ 0 & \Gamma_2 \end{pmatrix} \vec{x} \tag{3.40}$$

where $\bar{\kappa}(x) = m(x)/x^2$, and $m(x) = 2\int_0^x x' dx' \kappa(x')$.
Translate the origin of the source plane, $\vec{y} \to \vec{y} + \vec{\alpha}_p(0)$.

$$\Rightarrow \vec{y} = \vec{x}[1 - \bar{\kappa}(x)] - \begin{pmatrix} \Gamma_1 & 0 \\ 0 & \Gamma_2 \end{pmatrix} \vec{x} \, . \tag{3.41}$$

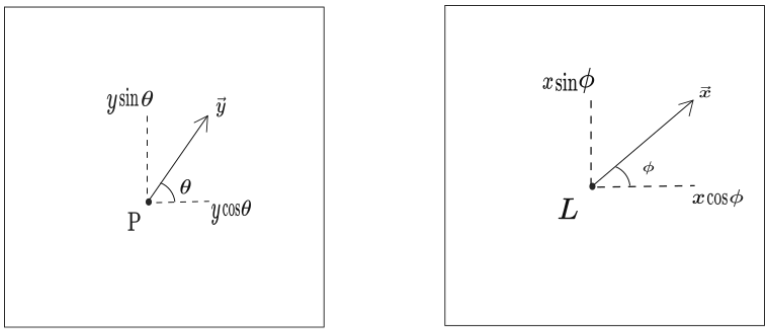

Figure 3.5: In the source plane and image plane the components of $\vec{y}$ and $\vec{x}$ are shown respectively.

In polar coordinates

$$\vec{y} = y(\cos\vartheta, \sin\vartheta) \,, \tag{3.42}$$
$$\vec{x} = x(\cos\varphi, \sin\varphi) \,. \tag{3.43}$$

The lens equation (3.41) can be rewritten as

$$y\cos\vartheta = x\cos\varphi[1 - \bar{\kappa}(x) - \Gamma_1] \,, \tag{3.44}$$
$$y\sin\vartheta = x\sin\varphi[1 - \bar{\kappa}(x) - \Gamma_2] \,. \tag{3.45}$$

Eliminating $\bar{\kappa}(x)$ from the above two equations gives,

$$x = \frac{2y\sin(\varphi - \vartheta)}{(\Gamma_2 - \Gamma_1)\sin 2\varphi} \,. \tag{3.46}$$

For a given source position (y, ϑ), $y > 0$, the solution (x, φ) can be geometrically found by considering the two curves,

$$u_1(\varphi) = \frac{\cos\varphi}{y} \quad ; \quad v_1(\varphi) = \frac{\sin\varphi}{y} \tag{3.47}$$

and,

$$u_2(x) = \frac{\cos\vartheta}{x[1 - \bar{\kappa}(x) - \Gamma_1]} \quad ; \quad v_2(x) = \frac{\sin\vartheta}{x[1 - \bar{\kappa}(x) - \Gamma_2]} \,. \tag{3.48}$$

The points (u, v) where the two curves intersect correspond to solutions of the lens equation.

There is another way to solve the lens equation (3.41). The quadrupole lens can be reduced to a one-dimensional equation by considering

$$\cos\varphi = \frac{y_1}{x[1 - \bar{\kappa}(x) - \Gamma_1]} \,, \tag{3.49}$$
$$\sin\varphi = \frac{y_2}{x[1 - \bar{\kappa}(x) - \Gamma_2]} \,, \tag{3.50}$$

and on adding the squares of the above two equations,

$$x^2[1 - \bar{\kappa}(x) - \Gamma_1]^2[1 - \bar{\kappa}(x) - \Gamma_2]^2 - y_1^2[1 - \bar{\kappa}(x) - \Gamma_2]^2 - y_2^2[1 - \bar{\kappa}(x) - \Gamma_1]^2 = 0 \,. \tag{3.51}$$

Solutions $x \geq 0$ yield all the image positions.

The Jacobian matrix is given as

$$A = \begin{pmatrix} 1 - \bar{\kappa}(x) - \Gamma_1 - \frac{x_1^2}{x}\bar{\kappa}'(x) & -\frac{x_1 x_2}{x}\bar{\kappa}'(x) \\ -\frac{x_1 x_2}{x}\bar{\kappa}'(x) & 1 - \bar{\kappa}(x) - \Gamma_2 - \frac{x_2^2}{x}\bar{\kappa}'(x) \end{pmatrix} \tag{3.52}$$

where the prime denotes differentiation with respect to x and

$$\det A = (1 - \bar{\kappa} - \Gamma_1)(1 - \bar{\kappa} - \Gamma_2) - x\bar{\kappa}'(1 - \bar{\kappa} - \Gamma_2 \cos^2\varphi - \Gamma_1 \sin^2\varphi) \, . \tag{3.53}$$

For $\det A = 0$, the critical curves satisfy the equation

$$\cos^2\varphi = \frac{1 - \bar{\kappa} - \Gamma_1}{\Gamma_1 - \Gamma_2}\left(\frac{1 - \bar{\kappa} - \Gamma_2}{x\bar{\kappa}'} - 1\right) \, . \tag{3.54}$$

Due to the symmetry of our lens model with respect to both reflections $(x_1, x_2) \mapsto \pm(x_1, -x_2)$, $(y_1, y_2) \mapsto \pm(y_1, -y_2)$, the corresponding value of $\cos^2\varphi$ yields four different critical points, one in each quadrant of the lens plane.

Thus in the case of perturbed symmetry, we introduce the perturbation effect by modifying the deflection angle by perturbed quadrupole term. The time delay between two images is evaluated by considering the modified deflection angle which accounts for the perturbation and considering the purely symmetric case for the second term in (2.74), so that it can be approximated as a point mass for $|\vec{x}|$ greater than mass distribution of lens.

$$\vec{\alpha}(\vec{x}) = \bar{\kappa}(x)\vec{x} + \begin{pmatrix} \Gamma_1 & 0 \\ 0 & \Gamma_2 \end{pmatrix}\vec{x} \tag{3.55}$$

$$(\vec{\alpha}(\vec{x}))^2 = [\bar{\kappa}(x)]^2 x^2 + 2\bar{\kappa}(x)(\Gamma_1 x_1^2 + \Gamma_2 x_2^2) + (\Gamma_1^2 x_1^2 + \Gamma_2^2 x_2^2) \tag{3.56}$$

where $\vec{x} = (x_1, x_2)$. So the time delay between two images at $\vec{x}^{(1)}$ and $\vec{x}^{(2)}$ is

$$c(t_1 - t_2) = \frac{D_d D_{ds}}{2D_s}\left(\frac{\xi_0 D_s}{D_d D_{ds}}\right)^2 \left[(\vec{\alpha}(\vec{x}^{(1)}))^2 - (\vec{\alpha}(\vec{x}^{(2)}))^2\right] + \frac{4G}{c^2}\int d^2\xi' \Sigma(\vec{\xi}') \ln\left(\frac{|\vec{\xi}^{(2)} - \vec{\xi}'|}{|\vec{\xi}^{(1)} - \vec{\xi}'|}\right) \tag{3.57}$$

$$\Rightarrow c(t_1 - t_2) = \frac{\xi_0^2}{2}\frac{D_s}{D_d D_{ds}}\left[(\vec{\alpha}(\vec{x}^{(1)}))^2 - (\vec{\alpha}(\vec{x}^{(2)}))^2\right] + \frac{4GM}{c^2}\ln\left|\frac{x^{(2)}}{x^{(1)}}\right| \tag{3.58}$$

Chapter 4

Mass Profile of Lenses

4.1 Singular Isothermal Sphere

A simple model describing the mass distribution of galaxies with spherically symmetric gravitational potential is the singular isothermal sphere (SIS). The three dimensional mass distribution is given as (Narayan and Bartelmann, 1996)

$$\rho(r) = \frac{\sigma_v^2}{2\pi G}\,\frac{1}{r^2}\ , \tag{4.1}$$

where $\rho(r)$ is the mass density within radius r, σ_v is the one dimensional velocity dispersion of the stars which is a constant for a galaxy and is related to the rotational velocity v_{rot} of the galaxy by the relation, $\sigma_v^2 = \frac{1}{2}v_{rot}^2$.
The projected surface mass density along the line-of-sight is obtained as

$$\Sigma(\xi) = \frac{\sigma_v^2}{2G}\,\frac{1}{\xi}\ , \tag{4.2}$$

where ξ is the distance from the center of the two dimensional profile. We choose,

$$\xi_0 = 4\pi\left(\frac{\sigma_v}{c}\right)^2\frac{D_d D_{ds}}{D_s}\ . \tag{4.3}$$

Thus,

$$\Sigma(x) = \frac{1}{2x}\Sigma_{cr}\ , \tag{4.4}$$

and the convergence for the singular isothermal sphere is

$$\kappa(x) = \frac{1}{2x}\ . \tag{4.5}$$

From (3.18), we obtain

$$\alpha(x) = \frac{x}{|x|}\ , \tag{4.6}$$

and the lens equation becomes,

$$y = x - \frac{x}{|x|}\ . \tag{4.7}$$

Consider $y > 0$.

(i) For $y < 1$, there are two images at $x = y + 1$ and $x = y - 1$.

(ii) For $y > 1$, there is only one image at $x = y + 1$.

The Jacobian is

$$A = \frac{dy}{dx} = 1 \ , \tag{4.8}$$

from the lens equation (4.7),

$$\frac{y}{x} = 1 - \frac{1}{|x|} = \frac{|x| - 1}{|x|} \ , \tag{4.9}$$

thus the magnification is

$$\mu = \frac{x}{y}\frac{dx}{dy} = \frac{|x|}{|x| - 1} \ . \tag{4.10}$$

The circle $|x| = 1$ is the tangential critical curve. From (3.27), the shear is

$$\gamma(x) = \frac{x}{x^2} - \frac{1}{2x} = \frac{1}{2x} = \kappa(x) \ . \tag{4.11}$$

If $y < 1$, the magnifications of the two images are

$$\mu_+ = \frac{y+1}{y} = 1 + \frac{1}{y} \ , \tag{4.12}$$

$$\mu_- = \frac{|y-1|}{|y-1|-1} = \frac{-y+1}{-y} = 1 - \frac{1}{y} \ . \tag{4.13}$$

For $y = 1$, the second image disappears, and for $y \to \infty$, the source magnification tends to unity. From (3.36), we obtain the deflection potential as,

$$\psi(x) = |x| \ , \tag{4.14}$$

and, from (2.75), the time delay between the two images as,

$$\begin{aligned} c\Delta t &= \xi_0^2 \frac{D_s}{D_d D_{ds}} \left(\frac{(y+1-y)^2}{2} - \frac{(y-1-y)^2}{2} - |y+1| + |y-1| \right) \\ &= \left[4\pi \left(\frac{\sigma_v}{c} \right)^2 \right]^2 \frac{D_d D_{ds}}{D_s} (-y - 1 - y + 1) \\ &= -\left[4\pi \left(\frac{\sigma_v}{c} \right)^2 \right]^2 \frac{D_d D_{ds}}{D_s} 2y \end{aligned} \tag{4.15}$$

where the '$-$' sign denotes that the image at $x_+ = y + 1$ reaches the observer earlier than the image at $x_- = y - 1$.

4.2 Exponential Disk

The mass distribution of spiral galaxy is usually described by the exponential disk. Disks are often modelled as idealised infinitely thin, radially exponential, collections of dust, gas and stars with surface density (Courteau et al., 2014)

$$\Sigma(\theta) = \Sigma_0 \exp(-\theta/\theta_0) \ , \tag{4.16}$$

where Σ_0 is the central surface mass density and θ_0 is the scale length of the lens model. The convergence becomes

$$\kappa(\theta) = \kappa_0 \exp(-\theta/\theta_0) \ . \tag{4.17}$$

The scaled deflection angle is obtained from (3.18) as,

$$\begin{aligned} \alpha(\theta) &= \frac{2}{\theta}\int_0^\theta \theta' d\theta' \kappa(\theta') \\ \Rightarrow \alpha(\theta) &= \frac{2\kappa_0}{\theta}[\theta_0^2 - \theta_0(\theta+\theta_0)\exp(-\theta/\theta_0)] \ , \end{aligned} \tag{4.18}$$

and the shear (3.27) as,

$$\begin{aligned} \gamma(\theta) &= \frac{1}{\theta}\alpha(\theta) - \kappa(\theta) \\ \Rightarrow \gamma(\theta) &= \frac{\kappa_0}{\theta^2}[2\theta_0^2 - (\theta^2 + 2\theta\theta_0 + 2\theta_0^2)\exp(-\theta/\theta_0)] \ . \end{aligned} \tag{4.19}$$

This is the case of face-on galaxy, and the lens equation for this case becomes

$$\beta = \theta - \frac{2\kappa_0}{\theta}[\theta_0^2 - \theta_0(\theta+\theta_0)\exp(-\theta/\theta_0)] \ . \tag{4.20}$$

The image position θ cannot be solved analytically (Wei et al., 2018).

4.3 Navarro-Frenk-White density profile

The density profile of dark matter halos numerically simulated by Navarro, Frenk and White (Navarro et al., 1997) in the framework of cold dark matter (CDM) cosmogony can be described well by the radial function

$$\rho(r) = \frac{\rho_s}{(r/r_s)(1+r/r_s)^2} \ , \tag{4.21}$$

within the halo mass range $3 \times 10^{11} \lesssim M_{200}/M_\odot \lesssim 3 \times 10^{15}$. The two parameters r_s and ρ_s are the scale radius and the characteristic density of the halo. NFW parametrized dark matter halos by their masses M_{200} which is defined as the masses enclosed within spheres of radius r_{200} in which the average density is 200 times the critical density for closure of the Universe (Meneghetti, 2019; Bartelmann, 1996; Golse and Kneib, 2002).
Choosing $\xi_0 = r_s$, the density profile (4.21) implies the surface mass density

$$\Sigma(x) = \frac{2\rho_s r_s}{x^2-1} f(x) \ , \tag{4.22}$$

with

$$f(x) = \begin{cases} 1 - \frac{2}{\sqrt{x^2-1}} \arctan\sqrt{\frac{x-1}{x+1}} & \text{for } x > 1 \\ 1 - \frac{2}{\sqrt{1-x^2}} \operatorname{arctanh}\sqrt{\frac{1-x}{1+x}} & \text{for } x < 1 \\ 0 & \text{for } x = 1 \end{cases} \ . \tag{4.23}$$

We define $\kappa_s \equiv \rho_s r_s \Sigma_{cr}^{-1}$, so the convergence can be written as

$$\kappa(x) = 2\kappa_s \frac{f(x)}{x^2 - 1} \,, \tag{4.24}$$

and the dimensionless mass is obtained as

$$m(x) = 4\kappa_s h(x) \,, \tag{4.25}$$

where

$$h(x) = \ln \frac{x}{2} + \begin{cases} \frac{2}{\sqrt{x^2-1}} \arctan \sqrt{\frac{x-1}{x+1}} & \text{for } x > 1 \\ \frac{2}{\sqrt{1-x^2}} \operatorname{arctanh} \sqrt{\frac{1-x}{1+x}} & \text{for } x < 1 \\ 1 & \text{for } x = 1 \end{cases} \,. \tag{4.26}$$

The lensing potential is given by

$$\psi(x) = 4\kappa_s g(x) \,, \tag{4.27}$$

where

$$g(x) = \frac{1}{2} \ln^2 \frac{x}{2} + \begin{cases} 2 \arctan^2 \sqrt{\frac{x-1}{x+1}} & \text{for } x > 1 \\ -2 \operatorname{arctanh}^2 \sqrt{\frac{1-x}{1+x}} & \text{for } x < 1 \\ 0 & \text{for } x = 1 \end{cases} \,, \tag{4.28}$$

and the deflection angle

$$\alpha(x) = \frac{4\kappa_s}{x} h(x) \,. \tag{4.29}$$

Chapter 5

A Survey of Gravitationally Lensed Systems

In this chapter we take a look at the different sky surveys and gravitational lensing projects. All the sky maps are generated with the astronomical software *Aladin sky atlas* developed at CDS, Strasbourg Observatory, France (Bonnarel et al., 2000; Boch and Fernique, 2014). Additionally, another software – *Topcat*[1] (Taylor, 2005) – played a crucial role to manipulate the large astronomical metadata, and create customized catalogues and VOTables.

5.1 Sky Surveys and Projects

CLASS (Cosmic Lens All-Sky Survey)

CLASS (Myers et al., 2003) has obtained high-resolution radio images of over 10,000 flat-spectrum radio sources. It is the largest and best-studied statistical sample of radio-loud gravitationally lensed systems. The survey was conducted over four observing 'seasons' from 1994 to 1999. Its primary goal was to identify lenses where multiple images are formed from compact flat-spectrum radio sources. During its run, CLASS observed 13,783 radio sources with the Very Large Array (VLA) at 8.4 GHz in its largest 'A'-configuration with resolution of 0.2 arcsecond. It covered a region between declination $0° - 75°$. CLASS selected sources from the Green Bank Survey (GB6) catalog at 4.85 GHz having a flux density of atleast 30 mJy. The selection was made by comparing this catalog with the 1.4 GHz NVSS. CLASS found 16 new gravitationally lensed systems. On combining with Jodrell Bank VLA Astronomical Survey (JVAS), the JVAS/CLASS survey contains a total of 22 lens systems.

CASTLES (CfA Arizona Space Telescope LEns Survey)

CASTLES[2] (Falco et al., 2001) is a dedicated gravitational lensing survey that exploits the sensitivity and resolution of the Hubble Space Telescope (HST) at optical and infrared wavelengths. It has produced a uniform sample of multi-band images of all known galaxy-mass lens systems and source images. These measurements

[1] `http://www.starlink.ac.uk/topcat/`

[2] `https://www.cfa.harvard.edu/castles/`

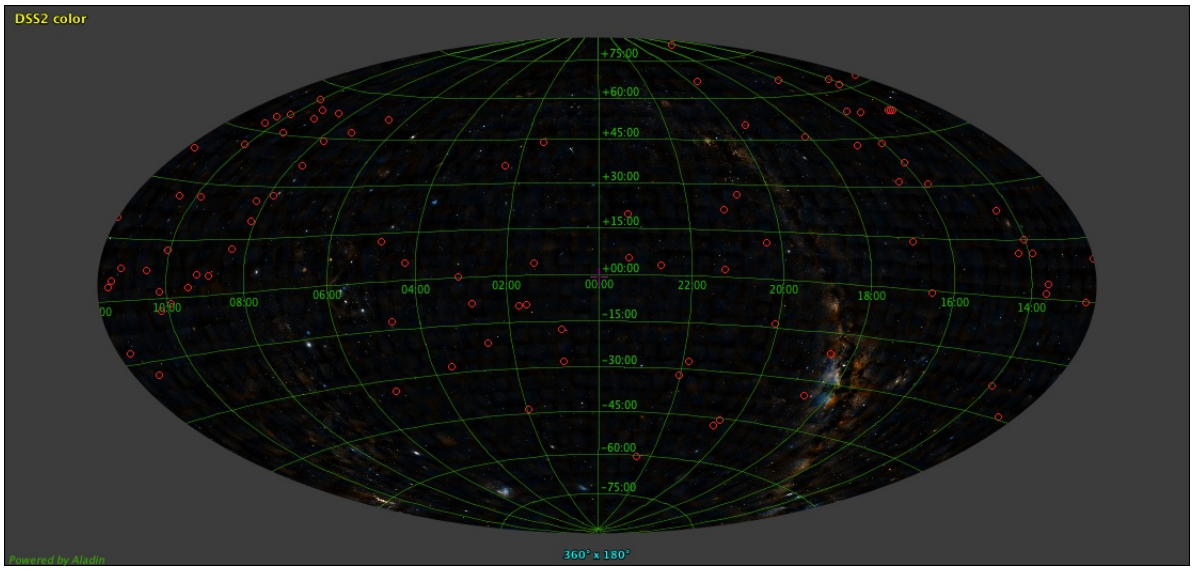

Figure 5.1: The distribution of lens systems found in CASTLES catalog is shown projected on DSS (Digital Sky Survey). The red circles mark the positions of each lens system.

are used to investigate the properties of dust and dark matter in lens galaxies, the evolution of lens galaxies and the cosmological model by refining constraints on the Hubble constant H_0.
The survey has recorded 100 gravitational lens systems (Fig. 5.1). The sources in this catalogue are either AGNs, quasars or galaxies which are lensed by a foreground galaxy. The typical separation between images of the source is around $1'' - 3''$. The CASTLES filters (V and I on WFPC2; H on NIC2) match the usual choices for studies of other galaxies at comparable redshifts. CASTLES began in HST Cycle 7, and continued through Cycles 8 and 9.

COSMOGRAIL (COSmological MOnitoring of GRAvItational Lenses)

COSMOGRAIL[3] (Courbin et al., 2005) project monitors strongly lensed quasars and is aimed at measuring time delays for most known lensed quasars, from optical light curves obtained with small-scale dedicated telescopes in the northern and southern hemispheres. The goal is to measure individual time delays with an accuracy below 3%, in order to determine the Hubble constant H_0. This is an ongoing project which started in April 2004. The most recent result of this project is a 2.4% determination of the Hubble constant, using the light curves of the lensed QSO HE0435-1223.
The project involves five telescopes – (i) the Swiss 1.2 m Euler telescope located at La Silla, Chile, (ii) the Swiss-Belgian 1.2 m Mercator telescope, located in the Canaria islands (La Palma, Spain), (iii) the 2 m robotic telescope of the Liverpool University, UK, also located at La Palma, (iv) the 1.5 m telescope of Maidank observatory in Uzbekistan, and (v) the 2 m Himalayan Chandra Telescope. COSMOGRAIL has given rise to several projects involved in measuring the Hubble constant, in particular H0LiCOW and STRIDES.

[3] `https://www.epfl.ch/labs/lastro/scientific-activities/cosmograil/`

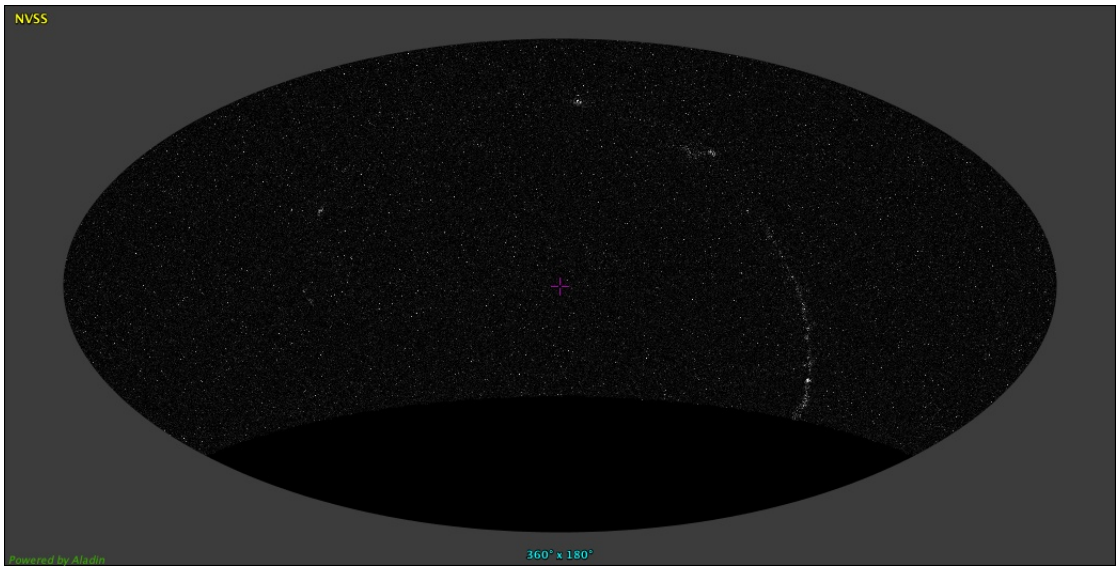

Figure 5.2: The sky coverage of NVSS is shown here.

NVSS (NRAO VLA Sky Survey)

The National Radio Astronomy Observatory (NRAO) Very Large Array (VLA) Sky Survey – the NVSS[4] catalog – covers the sky north of the J2000.0 declination of $-40°$ at 1.4 GHz (Condon et al., 1998). It covers 82% of the celestial sphere (see Fig. 5.1). The data was acquired in the compact D and DnC configurations of the VLA between 1993 September and 1996 October. Additional observations were made during the fourth quarter of 1997 to fill small gaps in this coverage. The complete NVSS is based on 217,446 "snapshot" observations of partially overlapping primary-beam areas, each of which was imaged separately. A source catalog was extracted from each image by filling elliptical Gaussians to all significant peaks. The principal data products are a set of 2326 $4° \times 4°$ continuum "cubes" with three planes containing Stokes I, Q, and U images and a catalogue of almost 2×10^6 discreet sources stronger than flux density $S \approx 2.5$ mJy. The images all have a full width between half-maximum (FWHM) angular resolution of $45''$ and nearly uniform sensitivity. The NVSS catalog provides the flux density of radio sources at 1.4 GHz along with the linearly polarized flux density. The rms uncertainties in right ascension and declination vary from < 1 arcsecond for relatively strong ($S > 15$ mJy) point sources to 7 arcsecond for the faintest ($S = 2.3$ mJy) detectable sources. Their rms brightness fluctuations are about 0.45 mJy/beam = 0.14 K (Stokes I) and 0.29 mJy/beam = 0.09 K (Stokes Q and U).

FIRST (Faint Images of the Radio Sky at Twenty cm)

The FIRST[5] survey began in 1993, and covers the north and south Galactic caps (Helfand et al., 2015). There are 946,432 sources in the catalog and the sky area covered is a total of about 10,575 square degrees of sky (8,444 square degrees in the north Galactic cap and 2,131 square degrees in the south Galactic cap). Over most of the survey area, the detection limit is 1 mJy. A region along the equatorial strip

[4] `https://www.cv.nrao.edu/nvss/`
[5] `http://sundog.stsci.edu/index.html`

(RA = 21.3 to 3.3 hrs, Dec = -1 to 1 deg) has a deeper detection threshold because two epochs of observation were combined. The typical detection threshold in this region is 0.75 mJy.
The FIRST survey acquired data using VLA in it's B-configuration from Spring 1993 through Spring 2004. Additional data in the southern Galactic cap were acquired in Spring 2009 and Spring 2011. The VLA was in a hybrid condition in 2009, with some new EVLA (Expanded VLA) receivers and some old VLA receivers. In 2011 the EVLA receivers were available with an early version of the new EVLA data system, so there are a number of differences from the old data:

Date	Frequencies	Bandpass	Integration
Before 2011	1365, 1435 MHz	2×7 3-MHz channels	180 seconds
2011	1335, 1730 MHz	2x64 2-MHz channels	60 seconds

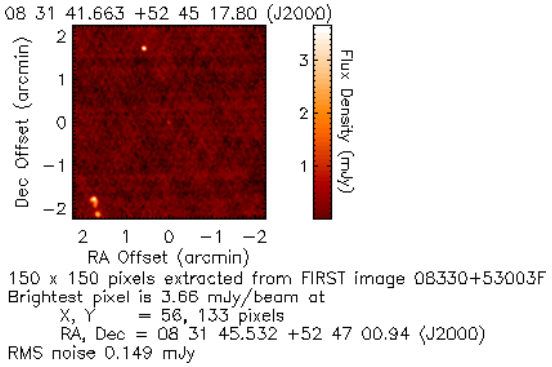

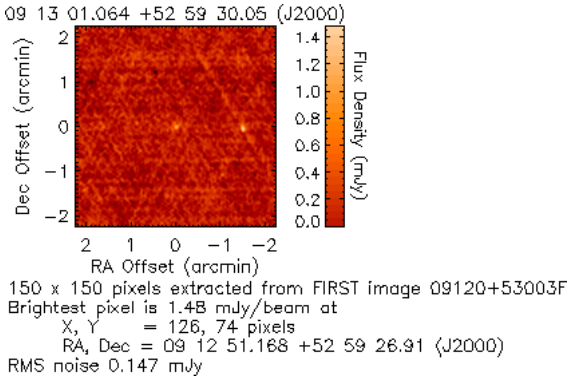

Figure 5.3: The final images from FIRST, produced by coadding the twelve images adjacent to each pointing center.

5.2 Gravitationally Lensed Quasar Catalog

In this section, a catalog of strong gravitationally lensed quasars with associated polarization flux density is produced. A concise catalog of all known gravitationally lensed quasars is made available on `https://research.ast.cam.ac.uk/lensedquasars/index.html`. There is one more lensed quasar system, B1152+200, found in CLASS/CASTLES which is not included in the mentioned catalog. This catalog (plus B1152+200) consisting of 221 lensed quasar systems is taken as the base catalog. Of these, the lens systems with recorded polarization are chosen. This is done by cross-matching the base catalog and the NVSS catalog with search radius of 10 arcseconds. This reduces the base catalog – now consisting of only lens systems with associated polarization flux density – to 42 (i.e., 41 +1) lens systems. These lensed quasars are listed in Table 5.1.
Table 5.1 lists the (i) Name: name of the lens system, (ii) Separation: this is the separation between the two images of the quasar, or if there are more than 2 images, then the maximum separation between two images, in arcseconds, (iii) N_{img}: the number of images of the quasar, where 0 refers to Einstein ring, 2 to double, 4 to quad, and so on, (iv) z_d: redshift of the deflector/lens, (v) z_s: redshift of the source, (vi) $S_{1.4}$: this is the integrated 1.4 GHz flux density of the radio source, in mJy, (vii) Polarization flux density: this is the integrated linearly polarized flux density, in mJy. The blank spaces in the table are the missing data that hasn't been recorded due to difficulty in measurements or inconclusive results.
As it was mentioned in the previous section, NVSS has a minimum radio flux density detection threshold of 2.5 mJy. So sources with flux density < 2.5 mJy are not included. FIRST catalog has a detection threshold of 1 mJy, or 0.75 mJy at some regions. To obtain a complete catalog of radio loud sources, a cross-match between the base catalog and FIRST catalog is conducted. Table 5.2 lists the systems which were not detected in NVSS but possess flux density at 1.4 GHz. However, it is still unknown whether these lens systems are linearly polarized or not.

Considering the rms brightness fluctuations of NVSS, we impose a limit on the polarization flux density. We choose only those systems with a polarization flux density greater than the rms noise, i.e., 0.35 mJy. Additionally, there exist some spurious polarized sources which must be excluded. We consider polarization leakage at 0.5% level. Thus, we set two selection criteria on Table 5.1,

(i) Polarization flux density, or Pol. flux > 0.35 mJy, and

(ii) $\frac{\text{Pol. flux}}{\text{Total flux, } S_{1.4}} > 0.005$.

Table 5.3 shows the lens systems fulfilling these two criteria. The highlighted lens systems are most likely to possess linear polarization.

Name	**Separation (in arcsec)**	N_{img}	z_d	z_s	$S_{1.4}$ **(in mJy)**	**Polarization flux density (in mJy)**
J1004+1229	1.54	2	0.95	2.65	11.8	-0.06
B1030+074	1.65	2	0.6	1.54	155.4	0.59
B1152+200	1.59	2	0.439	1.019	76.6	0.38
B1600+434	1.4	2	0.41	1.59	75.9	1.23
B0128+437	0.55	4		3.124	130.8	0.8
PMNJ0134-0931	0.73	5	0.77	2.216	919.1	2.32
B0218+357	0.34	2	0.68	0.96	1707.2	5.75
MG0414+0534	2.4	4	0.96	2.64	2086.3	1.85
B0445+123	1.35	2	0.557		40.5	2.38
B0631+519	1.16	2	0.62		96.3	0.37
B0712+472	1.46	4	0.41	1.34	25.3	0.39
B0739+366	0.53	2			27.4	0.25
B0850+054	0.68	2	0.59	1.14	85.0	-0.08
Q0957+561	6.26	2	0.36	1.41	551.4	12.91
SDSS1029+2623	22.5	4	0.55	2.197	6.4	-0.14
B1127+385	0.74	2			28.8	-0.12
RXJ1131-1231	3.8	4	0.295	0.658	28.8	-0.31
B1359+154	1.71	6		3.235	114.5	0.53
H1413+117	1.35	4		2.55	7.8	0.25
B1422+231	1.68	4	0.34	3.62	267.9	1.52
MG1549+3047	1.7	0	0.11	1.17	1249.2	1.67
B1555+375	0.42	4			33.9	-0.26
PMNJ1632-0033	1.47	2		3.424	218.8	
MG1654+1346	2.1	0	0.25	1.74	424.9	5.01
PKS1830-211	0.99	2	0.89	2.51	10896.3	11.19
PMNJ1838-3427	0.99	2	0.0	2.78	279.8	10.86
B1933+503	1.0	10	0.76	2.63	108.0	0.74
PMNJ2004-1349	1.18	2			79.3	0.35
MG2016+112	3.52	2	1.01	3.27	190.6	0.25
B2045+265	2.74	4	0.87	1.28	54.7	0.61
B2108+213	4.57	2			52.6	
B2114+022	1.31	2	0.32	0.59	136.6	-0.08
B2319+052	1.36	2	0.62	0.0	84.0	-0.23
J0013+5119	2.92	2		2.63	3.6	-0.24
PSJ0147+4630	3.26	4	0.678	2.377	11.8	-0.21
DESJ0340-2545	6.81	3		1.68	2.6	-0.33
PSJ0417+3325	1.68	2		1.41	109.2	3.68
SDSSJ0921+2854	1.89	2	0.445	1.41	3.4	-0.28
PSJ0949+4208	2.6	2	0.508	1.27	6.8	0.54
PSJ1831+5447	2.39	2		1.07	23.5	0.19
HS2209+1914	1.04	2		1.07	4.5	-0.03
WISE2329-1258	1.26	2		1.314	2.4	0.31

Table 5.1: A catalog of matched lensed quasars with NVSS. It consists of 42 lensed quasar systems. Under the column N_{img}, 0 refers to ring image (Einstein ring).

Name	**Separation (in arcsec)**	N_{img}	z_d	z_s	**Peak flux density at 1.4 GHz (in mJy)**	$S_{1.4}$ **(in mJy)**
SBS0909+532	1.11	2	0.830	1.378	1.09	3.45
APM08279+5255	0.38	3		3.87	1.3	0.92
FSC10214+4724	1.59	4	0.9?	2.286	1.37	1.75
FBQ1633+3134*	0.66	2	0.684?	1.518	1.79	2.07
FBQ0951+2635	1.10	2	0.260	1.247	1.48	2.03
SDSSJ0818+0601	1.15	2	1.01?	2.35	1.15	1.5

Table 5.2: A catalog of matched lensed quasars with FIRST.

Name	**Separation (in arcsec)**	N_{img}	z_d	z_s	**Time delay (in days)**	$S_{1.4}$ **(in mJy)**	**Polarization flux density (in mJy)**	$\frac{\textbf{Pol. flux}}{\textbf{Total flux } S_{1.4}}$
B1152+200	1.59	2	0.439	1.019		76.6	0.38	0.00496083550913838
B1600+434	1.4	2	0.41	1.59	51.0 ± 2.0	75.9	1.23	0.0162055335968379
B0128+437	0.55	4		3.124		130.8	0.8	0.00611620795107034
PMNJ0134-0931	0.73	5	0.77	2.216		919.1	2.32	0.00252420846480252
B0218+357	0.34	2	0.68	0.96	10.5 ± 0.4	1707.2	5.75	0.00336808809746954
MG0414+0534	2.4	4	0.96	2.64		2086.3	1.85	0.000886737286104587
B0445+123	1.35	2	0.557			40.5	2.38	0.0587654320987654
B0631+519	1.16	2	0.62			96.3	0.37	0.00384215991692627
B0712+472	1.46	4	0.41	1.34		25.3	0.39	0.0154150197628458
Q0957+561	6.26	2	0.36	1.41	417.0 ± 3.0	551.4	12.91	0.0234131302140007
B1359+154	1.71	6		3.235		114.5	0.53	0.00462882096069869
B1422+231	1.68	4	0.34	3.62	8.2 ± 2.0	267.9	1.52	0.00567375886524823
MG1549+3047	1.7	0	0.11	1.17		1249.2	1.67	0.00133685558757605
MG1654+1346	2.1	0	0.25	1.74		424.9	5.01	0.0117910096493293
PKS1830-211	0.99	2	0.89	2.51	26.0 ± 4.0	10896.3	11.19	0.00102695410368657
PMNJ1838-3427	0.99	2		2.78		279.8	10.86	0.0388134381701215
B1933+503	1.0	10	0.76	2.63		108.0	0.74	0.00685185185185185
PMNJ2004-1349	1.18	2				79.3	0.35	0.00441361916771753
B2045+265	2.74	4	0.87	1.28		54.7	0.61	0.0111517367458867
PSJ0417+3325	1.68	2		1.41		109.2	3.68	0.0336996336996337
PSJ0949+4208	2.6	2	0.508	1.27		6.8	0.54	0.0794117647058824

Table 5.3: A catalog of 21 gravitationally lensed quasars with linear polarization fulfilling selection criterion (i). The measured time delay is also mentioned for some lens systems. The 14 highlighted rows are the ones which satisfy both the selection criteria.

Sky Maps

In the following, the sky distribution of different catalogs is shown in equatorial coordinates (Fig. 5.4, 5.5, 5.6). The distribution is projected on the NVSS intensity coverage map. The two maps in each figure show the same distribution. The difference being that the *bottom figure* in each also show the coordinates.

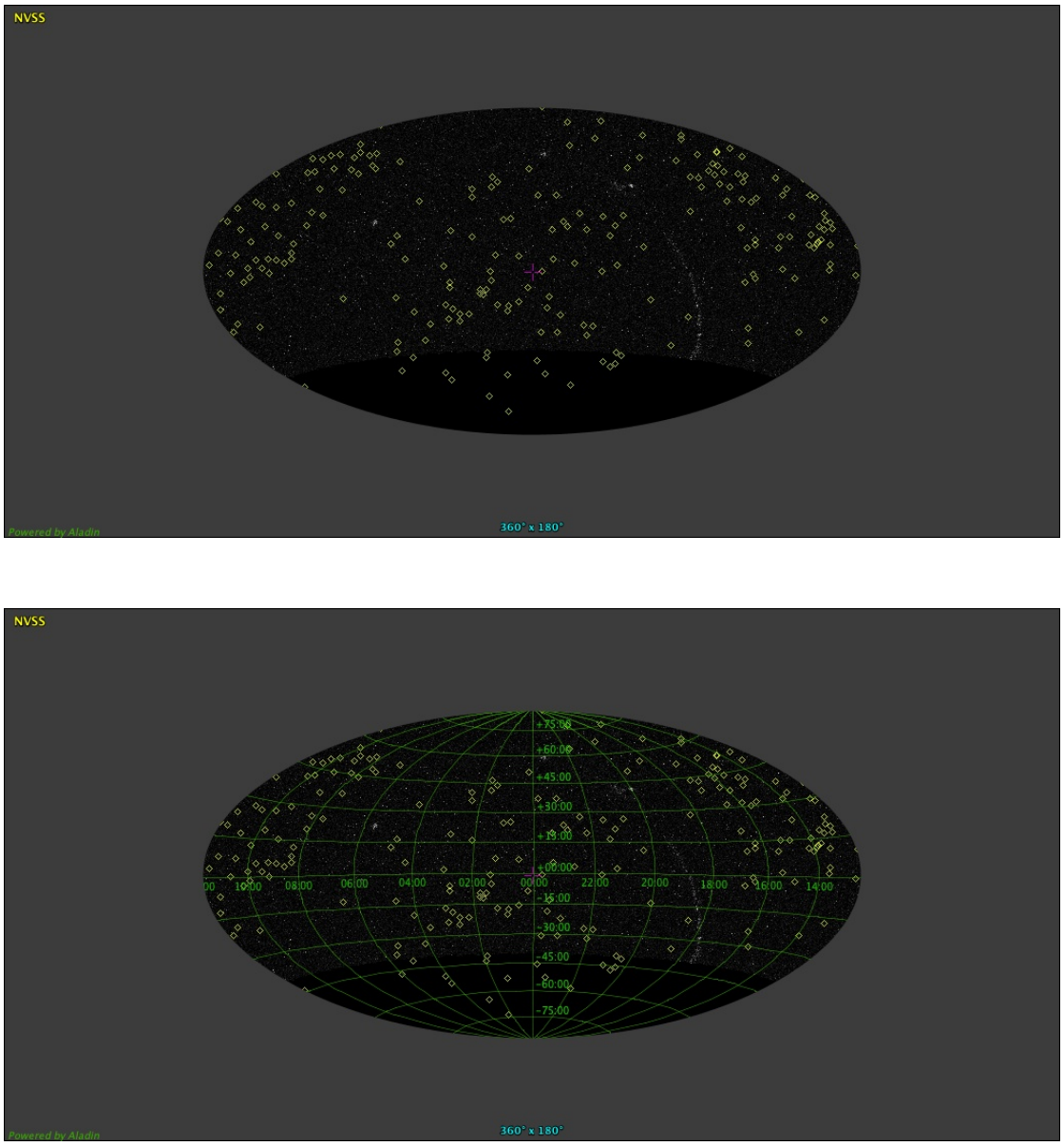

Figure 5.4: The figures show the distribution of the base catalog consisting of 221 lens systems. The distribution is almost uniform.

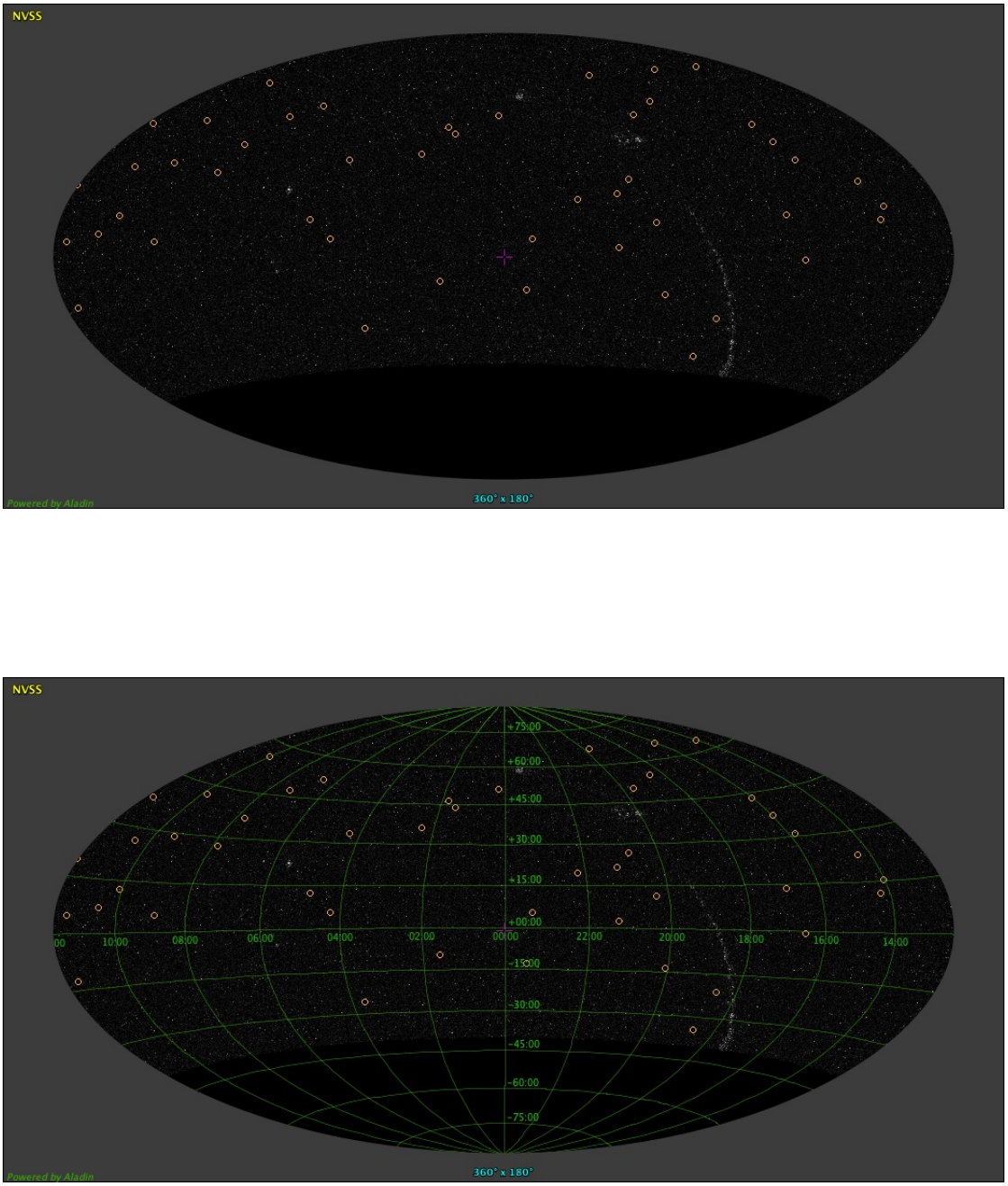

Figure 5.5: The 42 lens systems of Table 5.1 are shown here.

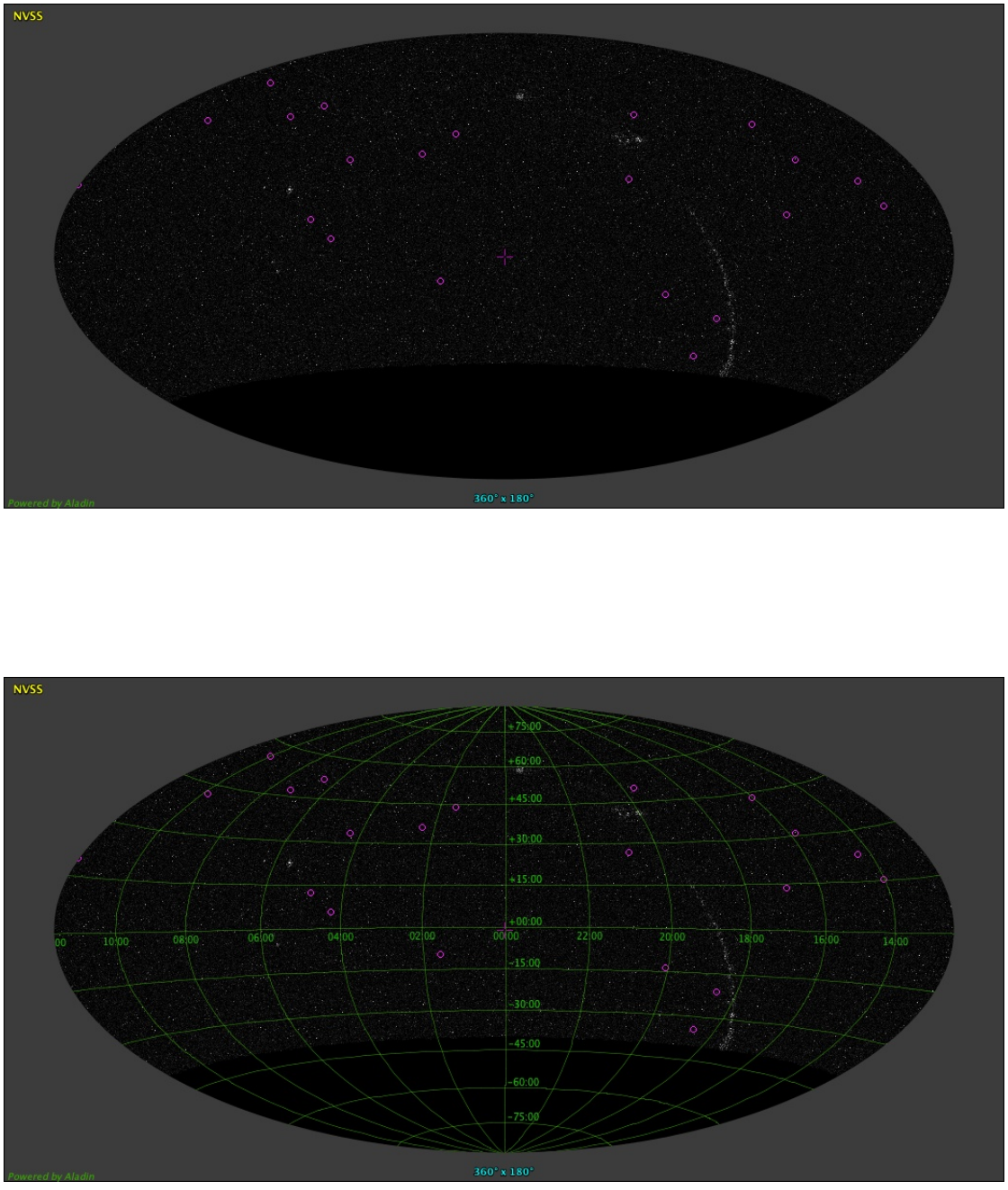

Figure 5.6: The 21 lens systems of Table 5.3 are shown here.

Histograms

Histograms of the final Table 5.3 are plotted here in Fig. 5.7 and Fig. 5.8.

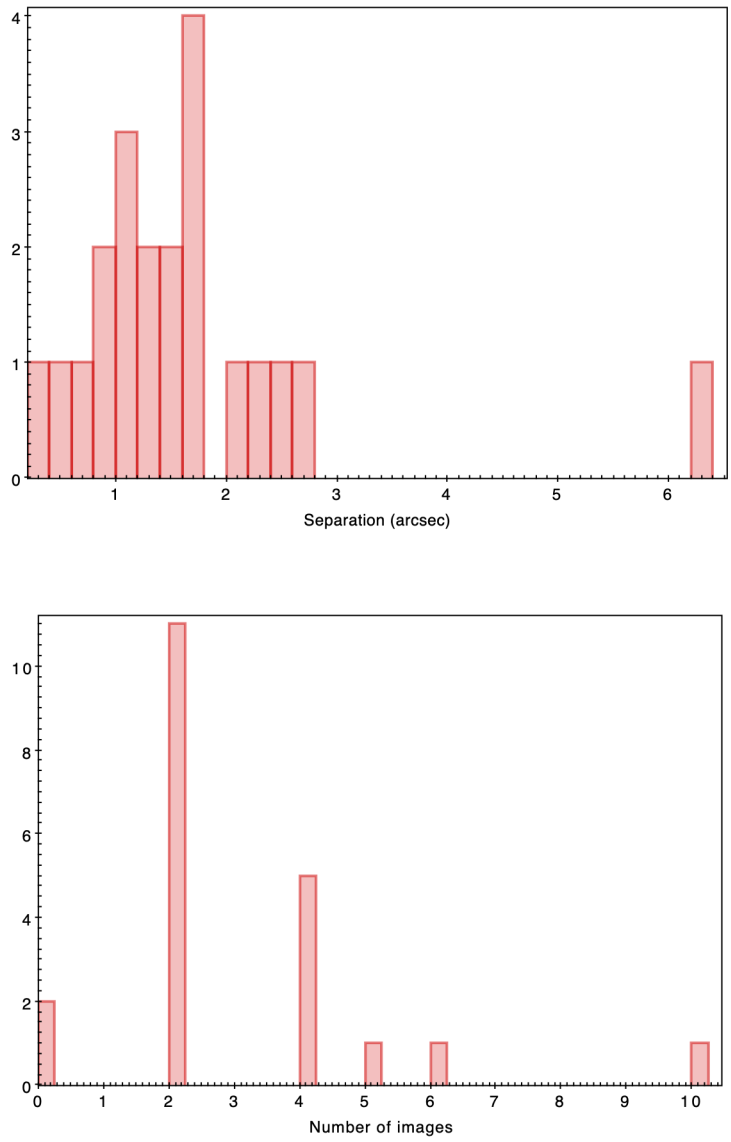

Figure 5.7: The *top figure* shows the histogram of the separation between images in arcseconds. The separation between images for most of the lenses is less than 3 arcsonds. The *bottom figure* shows the histogram of the number of images. Majority of the lenses are double or quad. As mentioned before, 0 denotes ring image.

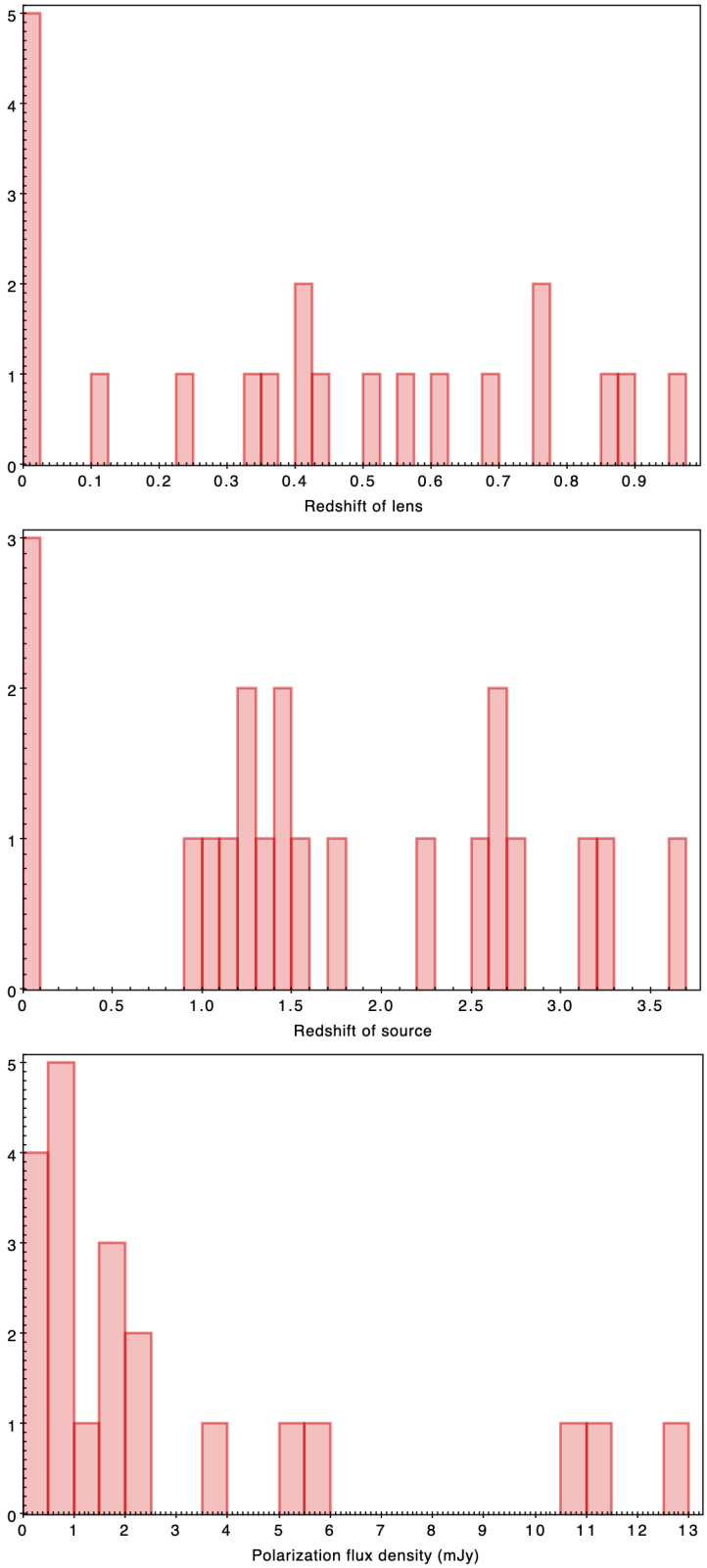

Figure 5.8: The *top figure* shows the distribution of redshift of lens galaxy. The *middle figure* shows the distribution of redshift of source quasar. In both these distributions the bar at 0 denotes the number of lens systems with missing redshift data. The *bottom figure* is the histogram of linearly polarized flux density in mJy.

Chapter 6

Conclusion

During the span of this thesis, I studied the analysis of time delay between two images of a source (section 2.2.4). It was observed that to calculate the time delay the relative positions of images, the lensing potential and the redshift of the lens must be known (eq. 2.75, 2.85). To obtain the lensing potential, a mass distribution of the lens has to be assumed. There are several mass density profiles for galaxies found in the literature. In chapter 4, a few of them are considered. A concise catalog of different mass models can be found in Keeton (2001). In chapter 3, it has been seen that axially symmetric lens models are relatively simpler to analyse than asymmetric models. In reality, most of the lenses are asymmetric and can be modelled as perturbed symmetric lenses.

A literature survey of gravitationally lensed systems was conducted in chapter 5. From the surveys search coverage and detection, it is noted that gravitational lensing is a rare phenomenon. There are a few hundreds of lensed systems recorded till date. There are some on-going collaborations and projects involved in time delay cosmography where precise time delay measurements are being calculated.

In section 5.2, I took a closer look at gravitationally lensed quasars. A uniform distribution of these lenses was observed in fig. 5.4. In the end, a catalog of known gravitationally lensed quasars (Table 5.3) with associated polarization was produced. With the present available data, I found 14 candidate lensed quasars with possible polarization.

Bibliography

N. Aghanim, Y. Akrami, M. Ashdown, J. Aumont, C. Baccigalupi, M. Ballardini, A. J. Banday, R. B. Barreiro, N. Bartolo, and et al. Planck 2018 results. *Astronomy and Astrophysics*, 641:A6, Sep 2020. doi: 10.1051/0004-6361/201833910.

M. Bartelmann. Arcs from a universal dark-matter halo profile. *Astronomy and Astrophysics*, 313:697–702, September 1996.

Aritra Basu, Jishnu Goswami, Dominik J. Schwarz, and Yuko Urakawa. Searching for axion-like particles under strong gravitational lenses. *arXiv e-prints*, art. arXiv:2007.01440, July 2020.

Gianfranco Bertone and Dan Hooper. History of dark matter. *Reviews of Modern Physics*, 90(4):045002, October 2018. doi: 10.1103/RevModPhys.90.045002.

R. D. Blandford and R. Narayan. Cosmological applications of gravitational lensing. *Annual Review of Astronomy and Astrophysics*, 30:311–358, January 1992. doi: 10.1146/annurev.astro.30.1.311.

T. Boch and P. Fernique. Aladin Lite: Embed your Sky in the Browser. In N. Manset and P. Forshay, editors, *Astronomical Data Analysis Software and Systems XXIII*, volume 485 of *Astronomical Society of the Pacific Conference Series*, page 277, May 2014.

F. Bonnarel, P. Fernique, O. Bienaymé, D. Egret, F. Genova, M. Louys, F. Ochsenbein, M. Wenger, and J. G. Bartlett. The ALADIN interactive sky atlas. A reference tool for identification of astronomical sources. *Astronomy and Astrophysics, Supplement*, 143:33–40, April 2000. doi: 10.1051/aas:2000331.

G. Carosi, A. Friedland, M. Giannotti, M. J. Pivovaroff, J. Ruz, and J. K. Vogel. Probing the axion-photon coupling: phenomenological and experimental perspectives. A snowmass white paper. *arXiv e-prints*, art. arXiv:1309.7035, September 2013.

Cervantes-Cota, Galindo-Uribarri, and Smoot. The Legacy of Einstein's Eclipse, Gravitational Lensing. *Universe*, 6(1):9, December 2019. doi: 10.3390/universe6010009.

J. J. Condon, W. D. Cotton, E. W. Greisen, Q. F. Yin, R. A. Perley, G. B. Taylor, and J. J. Broderick. The NRAO VLA Sky Survey. *Astronomical Journal*, 115(5):1693–1716, May 1998. doi: 10.1086/300337.

F. Courbin, A. Eigenbrod, C. Vuissoz, G. Meylan, and P. Magain. COSMOGRAIL: the COSmological MOnitoring of GRAvItational Lenses. In Yannick Mellier and Georges Meylan, editors, *Gravitational Lensing Impact on Cosmology*, volume 225, pages 297–303, June 2005. doi: 10.1017/S1743921305002097.

Stéphane Courteau, Michele Cappellari, Roelof S. de Jong, Aaron A. Dutton, Eric Emsellem, Henk Hoekstra, L. V. E. Koopmans, Gary A. Mamon, Claudia Maraston, Tommaso Treu, and Lawrence M. Widrow. Galaxy masses. *Reviews of Modern Physics*, 86(1):47–119, January 2014. doi: 10.1103/RevModPhys.86.47.

Michael Dine, Willy Fischler, and Mark Srednicki. A simple solution to the strong cp problem with a harmless axion. *Physics Letters B*, 104(3):199–202, 1981. doi: 10.1016/0370-2693(81)90590-6.

E. E. Falco, C. S. Kochanek, J. Lehár, B. A. McLeod, J. A. Muñoz, C. D. Impey, C. Keeton, C. Y. Peng, and H. W. Rix. The CASTLES Gravitational Lensing Tool. In Tereasa G. Brainerd and Christopher S. Kochanek, editors, *Gravitational Lensing: Recent Progress and Future Go*, volume 237 of *Astronomical Society of the Pacific Conference Series*, page 25, January 2001.

G. Golse and J. P. Kneib. Pseudo elliptical lensing mass model: Application to the NFW mass distribution. *Astronomy and Astrophysics*, 390:821–827, August 2002. doi: 10.1051/0004-6361:20020639.

I.S. Gradshteyn and I.M. Ryzhik. *Table of integrals, series, and products: Seventh edition*. Elsevier/Academic Press, Amsterdam, 2007.

David J. Helfand, Richard L. White, and Robert H. Becker. The Last of FIRST: The Final Catalog and Source Identifications. *Astrophysical Journal*, 801(1):26, March 2015. doi: 10.1088/0004-637X/801/1/26.

Charles R. Keeton. A Catalog of Mass Models for Gravitational Lensing. *arXiv e-prints*, art. astro-ph/0102341, February 2001.

David J. E. Marsh. Axion cosmology. *Physics Reports*, 643:1–79, July 2016. doi: 10.1016/j.physrep.2016.06.005.

Massimo Meneghetti. Introduction to gravitational lensing. *Lecture note*, 2019.

C. W. Misner, K. S. Thorne, and J. A. Wheeler. *Gravitation*. W. H. Freeman, San Francisco, 1973.

S. T. Myers, N. J. Jackson, I. W. A. Browne, A. G. de Bruyn, T. J. Pearson, A. C. S. Readhead, P. N. Wilkinson, A. D. Biggs, R. D. Blandford, C. D. Fassnacht, L. V. E. Koopmans, D. R. Marlow, J. P. McKean, M. A. Norbury, P. M. Phillips, D. Rusin, M. C. Shepherd, and C. M. Sykes. The Cosmic Lens All-Sky Survey - I. Source selection and observations. *Monthly Notices of the Royal Astronomical Society*, 341(1):1–12, May 2003. doi: 10.1046/j.1365-8711.2003.06256.x.

Ramesh Narayan and Matthias Bartelmann. Lectures on Gravitational Lensing. *arXiv e-prints*, art. astro-ph/9606001, June 1996.

Julio F. Navarro, Carlos S. Frenk, and Simon D. M. White. A Universal Density Profile from Hierarchical Clustering. *Astrophysical Journal*, 490(2):493–508, December 1997. doi: 10.1086/304888.

R. D. Peccei and Helen R. Quinn. CP conservation in the presence of pseudoparticles. *Phys. Rev. Lett.*, 38:1440–1443, Jun 1977. doi: 10.1103/PhysRevLett.38.1440.

S. Refsdal. The gravitational lens effect. *Monthly Notices of the Royal Astronomical Society*, 128:295, January 1964. doi: 10.1093/mnras/128.4.295.

Peter Schneider, Juergen Ehlers, and Emilio E. Falco. *Gravitational Lenses*. Springer, 2nd printing edition, 1999.

S. H. Suyu, V. Bonvin, F. Courbin, C. D. Fassnacht, C. E. Rusu, D. Sluse, T. Treu, K. C. Wong, M. W. Auger, X. Ding, S. Hilbert, P. J. Marshall, N. Rumbaugh, A. Sonnenfeld, M. Tewes, O. Tihhonova, A. Agnello, R. D. Blandford, G. C. F. Chen, T. Collett, L. V. E. Koopmans, K. Liao, G. Meylan, and C. Spiniello. H0LiCOW - I. H_0 Lenses in COSMOGRAIL's Wellspring: program overview. *Monthly Notices of the Royal Astronomical Society*, 468(3):2590–2604, July 2017. doi: 10.1093/mnras/stx483.

M. B. Taylor. TOPCAT & STIL: Starlink Table/VOTable Processing Software. In P. Shopbell, M. Britton, and R. Ebert, editors, *Astronomical Data Analysis Software and Systems XIV*, volume 347 of *Astronomical Society of the Pacific Conference Series*, page 29, December 2005.

D. Walsh, R. F. Carswell, and R. J. Weymann. 0957+561 A, B: twin quasistellar objects or gravitational lens? *Nature*, 279:381–384, May 1979. doi: 10.1038/279381a0.

Cheng-Liang Wei, Zhe Chu, and Yi-Ping Shu. The magnification invariant of circularly-symmetric lens models. *Research in Astronomy and Astrophysics*, 18 (7):080, July 2018. doi: 10.1088/1674-4527/18/7/80.

F. Wilczek. Problem of strong p and t invariance in the presence of instantons. *Phys. Rev. Lett.*, 40:279–282, Jan 1978. doi: 10.1103/PhysRevLett.40.279.

P.A. Zyla, R.M. Barnett, J Beringer, O Dahl, and et al. *(Particle Data Group), Prog. Theor. Exp. Phys. 2020, 083C01.* 2020.

Acknowledgement

I would like to thank my supervisor, Dominik Schwarz, for his guidance and encouragement throughout the period of my thesis. I would also like to thank Aritra Basu for his discussions and clarifications.

I acknowledge the financial support provided by the International Office Universität Bielefeld for the completion of my master's thesis.

I would also like to extend my thanks to my colleagues and staff in the Physics Department, in particular Susi Reder and Irene Kehler for all their assistance.

Lastly, I thank my parents for their constant support and patience.

Declaration of Authorship

I hereby certify that the thesis I am submitting is entirely my own original work except where otherwise indicated. I am aware of the University's regulations concerning plagiarism, including those regulations concerning disciplinary actions that may result from plagiarism. Any use of the works of any other author, in any form, is properly acknowledged at their point of use.

Date, Place

Shivani Deshmukh